Journal of Computational Physics 230 (2011) 61–86

Contents lists available at ScienceDirect

Journal of Computational Physics

journal homepage: www.elsevier.com/locate/jcp

Characteristics of an envelope model for laser–plasma accelerator simulation

Benjamin M. Cowan [a,*], David L. Bruhwiler [a], Estelle Cormier-Michel [a,b], Eric Esarey [b], Cameron G.R. Geddes [b], Peter Messmer [a], Kevin M. Paul [a]

[a] Tech-X Corporation, Boulder, CO 80303, United States
[b] LOASIS Program, Lawrence Berkeley National Laboratory, Berkeley, CA 94720, United States

ARTICLE INFO

Article history:
Received 1 January 2010
Received in revised form 15 June 2010
Accepted 6 September 2010
Available online 15 September 2010

Keywords:
Plasma accelerator
Laser–plasma acceleration
Laser wakefield acceleration
PIC
Envelope model

ABSTRACT

Simulation of laser–plasma accelerator (LPA) experiments is computationally intensive due to the disparate length scales involved. Current experiments extend hundreds of laser wavelengths transversely and many thousands in the propagation direction, making explicit PIC simulations enormously expensive and requiring massively parallel execution in 3D. Simulating the next generation of LPA experiments is expected to increase the computational requirements yet further, by a factor of 1000. We can substantially improve the performance of LPA simulations by modeling the envelope evolution of the laser field rather than the field itself. This allows for much coarser grids, since we need only resolve the plasma wavelength and not the laser wavelength, and therefore larger timesteps can be used. Thus an envelope model can result in savings of several orders of magnitude in computational resources. By propagating the laser envelope in a Galilean frame moving at the speed of light, dispersive errors can be avoided and simulations over long distances become possible. The primary limitation to this envelope model is when the laser pulse develops large frequency shifts, and thus the slowly-varying envelope assumption is no longer valid. Here we describe the model and its implementation, and show rigorous benchmarks for the algorithm, establishing second-order convergence and correct laser group velocity. We also demonstrate simulations of LPA phenomena such as self-focusing and meter-scale acceleration stages using the model.

© 2010 Elsevier Inc. All rights reserved.

1. Introduction

Laser-driven plasma-based accelerators (LPAs) [1,2] are capable of producing accelerating gradients orders of magnitude higher than conventional accelerators. In an LPA, the ponderomotive force from a relativistic laser field drives electrons in a plasma away from the region of high intensity. This excites a longitudinal oscillation—a *wakefield*—in the plasma, which can sustain accelerating gradients into the tens to hundreds of GV/m. An electron bunch co-propagating with the plasma wave at the correct phase will be accelerated.

The intensity of the laser pulse is characterized by the normalized vector potential $a_0 = eA_0/mc$, where $-e$ and m are the electron charge and mass, respectively, and A_0 is the peak value of the vector potential of the laser field. For a monochromatic field, this is equal to

* Corresponding author. Tel.: +1 303 996 7521; fax: +1 303 448 7756.
E-mail addresses: benc@txcorp.com (B.M. Cowan), bruhwile@txcorp.com (D.L. Bruhwiler), ecormier@txcorp.com (E. Cormier-Michel), EHEsarey@lbl.gov (E. Esarey), CGRGeddes@lbl.gov (C.G.R. Geddes), messmer@txcorp.com (P. Messmer), kpaul@txcorp.com (K.M. Paul).

0021-9991/$ - see front matter © 2010 Elsevier Inc. All rights reserved.
doi:10.1016/j.jcp.2010.09.009

$$a_0 = \frac{eE\lambda}{2\pi mc^2}, \tag{1}$$

where E and λ are the peak electric field and wavelength of the laser. A relativistic laser field is defined by $a_0 \gtrsim 1$; this condition implies that an electron can be accelerated to relativistic velocities in a single optical cycle. A key parameter of the plasma wave is the characteristic plasma wavelength $\lambda_p = \sqrt{\pi/nr_e}$, where n is the plasma number density and $r_e = e^2/4\pi\epsilon_0 mc^2$ is the classical electron radius. The plasma wave oscillates at the associated plasma frequency; in the linear regime, where $a_0 \ll 1$, the angular frequency of the plasma wave is $\omega_p = 2\pi c/\lambda_p$. In the typical regimes of LPA operation, nonlinear effects cause the wave oscillation frequency to decrease [3]. In this paper we will consider in detail the special case of laser wakefield acceleration (LWFA), in which the plasma wake is driven by a single short laser pulse. In order to drive the plasma wake most efficiently, the laser pulse length must be on the order of λ_p [2].

Laser–plasma acceleration uses plasmas which are underdense with respect to the laser pulse, which means that $\lambda_p \gg \lambda$. In this case, the laser field propagates through the plasma with group velocity approximately $v_g = c(1 - \lambda_p^2/\lambda^2)^{1/2}$ in the 1D limit, assuming $a_0 \ll 1$. Because the plasma wave is driven by the laser field, the laser group velocity is also the plasma wave phase velocity. A highly relativistic electron bunch moving at $\sim c$ will therefore advance with respect to the plasma wave phase moving at $v_g < c$, and after a sufficiently long propagation distance will leave the accelerating phase of the wake. This process is called *dephasing*, and is one limitation on the length of an LPA stage. Another limitation is laser pulse *depletion*, in which the laser pulse loses energy and redshifts. Both these limitations will be discussed further in subsequent sections; see [2] for a detailed review of LPA physics.

Several years ago, high-quality electron beams were produced by self-trapping and accelerated to ~100 MeV in a few millimeters [4–6]. Since then, efforts have focused on obtaining beams useful for high-energy particle colliders [7] and radiation sources [8–11]. This involves developing longer acceleration stages to achieve greater total energy gain, and controlling the injection process for higher beam quality. Recently, acceleration to 1 GeV in a few centimeters was demonstrated [12]. In addition, experiments have shown that the quality of the electron beam can be improved by tailoring the plasma density profile in the injection process separately from the accelerating structure [13] or using colliding laser pulses [14]. For a high-energy collider, studies indicate the need to stage many LPA modules, each on the order of 1 m in length and achieving ~10 GeV of energy gain [7].

Simulations have played a significant role the development of LPAs. In particular, the particle-in-cell (PIC) method, a well-established algorithm for self-consistently modeling charged particles in electromagnetic fields [15,16], has been critical to the understanding of the LPA processes. The PIC algorithm discretizes the values of the electromagnetic fields in space and time on a Yee grid [17]. The Maxwell equations

$$\frac{\partial \mathbf{B}}{\partial t} = -\nabla \times \mathbf{E}, \quad \frac{\partial \mathbf{E}}{\partial t} = c^2 \nabla \times \mathbf{B} - \frac{1}{\epsilon_0}\mathbf{J} \tag{2}$$

are updated explicitly according to the finite-difference time-domain (FDTD) method [18]. The laser wavelength typically used in LPA experiments is $\lambda = 800$ nm; this must be well-resolved in a PIC simulation, and because of the Courant–Friedrichs–Levy (CFL) limit [18], the time step must then be a small fraction of a laser oscillation period.

It is also important for LPA simulations to capture the kinetic effects of the plasma particles in order to model the injection of beams into a plasma wake and the creation of dark current in accelerating stages. Thus, the PIC algorithm also treats the phase space coordinates of each particle explicitly. The particle momenta are updated using the Lorentz force equation

$$\frac{d\mathbf{p}}{dt} = q(\mathbf{E} + \mathbf{v} \times \mathbf{B}), \tag{3}$$

and the particle positions are then updated using $d\mathbf{x}/dt = \mathbf{p}/\gamma$, where γ is the Lorentz factor associated with the particle's momentum. The PIC method models particle kinetics by converting quantities between the discrete spatial grid and the continuous particle position space in order to define the electromagnetic fields at the particle positions and to define the electric current density $\mathbf{J}$ on the FDTD grid. Fields are interpolated to particle positions using linear weighting or higher-order splines. The current from the particles is deposited on the grid using the first-order charge-conserving scheme of Villasenor and Buneman [19] or the higher-order method of Esirkepov [20] to reduce numerical noise; for best performance the same weighting functions are used for interpolation and deposition. The PIC algorithm is well established, having been used extensively over the past several decades.

Future explorations of laser–plasma acceleration present difficulties for PIC simulations, due to the disparate length scales involved. The next generation of experiments will extend the accelerating stage length to ~1 m for ~10 GeV of energy gain. Since the stage length is limited by the dephasing length $L_d \sim \lambda_p^3/\lambda^2$, those experiments will use lower plasma density, and hence larger λ_p, to allow acceleration over this length, and correspondingly longer laser pulses. The transverse and longitudinal dimensions of the simulation domain scale as λ_p. Thus the simulations would have to encompass many thousands of cells longitudinally and hundreds transversely, and run for tens of millions of timesteps. For example, a plasma density of $n = 10^{23}$ m^{-3} gives a plasma wavelength of $\lambda_p = 106$ μm and a dephasing length of 1.8 m; the stage length is in fact limited to 0.9 m in order for the particle bunch to remain in the focusing phase of the transverse wake. For typical PIC simulation parameters, this would require about 10,000 grid cells longitudinally, 2500 in each transverse dimension, and over 50 million time steps. This is intractable even in two dimensions [21]. While the injection process in an LPA occurs over a shorter

distance, running PIC simulations of the injection process in 3D is expensive enough to make parameter studies for beam quality optimization quite difficult.

New tools are therefore needed to perform these simulations more quickly while preserving as much as possible of the physics modeled by PIC. Approximations to the full particle and field dynamics have been explored, both for theoretical insight and to ease computational burden. The quasi-static approximation [3] assumes that in a Galilean frame co-propagating along with the laser pulse at c, the laser field, plasma density, and associated wakefield change on the time scale of $\lambda_p^2/\lambda c$ (in 1D, or x_R/c in 3D with x_R the Rayleigh length), so that the laser period, and even a plasma period, need not be resolved in time. The quasi-static approximation has been implemented in several codes, including the fluid code LEM [22] and the particle codes WAKE [23] and QUICKPIC [24]. In addition, these codes applied the envelope approximation, in which the slowly-varying envelope of the laser pulse is modeled, rather than the laser field itself. This removes the need to spatially resolve the laser wavelength.

An alternative approach to resolving the disparity in length scales is the use of a Lorentz frame moving in the direction of the laser pulse [25–29]. For normalized boost velocity β and Lorentz parameter γ, the laser wavelength extends by a factor $\gamma(1+\beta)$ while the plasma length contracts by γ, potentially yielding speedups on the order of γ^2. This method does not make any approximations to the physics of the model, and speedups of several orders of magnitude have been reported in [27]. However, this approach suffers from noise buildup, possibly due to unresolved backscattered radiation, and rigorous tests have demonstrated a speedup factor of only $\sim$20 [28]. Although this approach is an exciting possibility, with full 3D PIC simulations of 10 GeV LPA stages estimated to require over 1 billion CPU hours, the available speedup is at present insufficient for this problem.

Another laboratory-frame algorithm has been implemented which retains the envelope approximation, but relaxes the quasi-static approximation somewhat. In that algorithm, the plasma period was temporally resolved, and the electromagnetic fields, rather than the vector potential, were used to model the wakefield. In addition, quantities were modeled in the lab frame, rather than the speed-of-light frame; this was implemented in the code turboWAVE [30]. Retaining the envelope approximation allowed a coarsening of the longitudinal grid by a factor of λ_p/λ versus full PIC, and consequently an increase in the time step by a similar factor. Thus a speedup of $(\lambda_p/\lambda)^2$ over explicit PIC is possible. In addition, temporally resolving the plasma period allowed modeling of kinetic effects which occur on that time scale, such as particle trapping, not modeled by the quasi-static method.

The algorithm was implemented in the plasma simulation code VORPAL [31] and tested in limited cases [32]. More recently, an improvement was made to the algorithm in order to resolve problems which appeared with long propagation distances, and implemented in turboWAVE [33]. In this article, we explore this improved algorithm using its implementation in VORPAL. First, we describe the numerical implementation of the algorithm. We then present some benchmark tests of the algorithm for convergence, laser group velocity accuracy, and numerical kinetic effects. Finally, we show benchmarks against explicit PIC for simulations of LWFA accelerator stages. We show that the model enables simulations of meter-scale stages important to next-generation experiments. We also remark on the computation time advantages of the envelope model with respect to explicit PIC. For clarity, we describe the theory behind the envelope approximation in detail in an appendix.

2. Numerical implementation

The numerical implementation of the envelope model is based on those in [33,32], but with several important differences. As in those references, the laser field is modeled by a complex scalar field a which represents the modulation on the sinusoidal oscillation of a single component of the transverse vector potential. Specifically, the transverse vector potential in the Coulomb gauge is given in terms of a by $\tilde{\mathbf{A}} = \hat{\epsilon} a$, where $\tilde{\mathbf{A}}$ is defined in Eq. (51) in the appendix and $\hat{\epsilon}$ is a constant polarization vector with $|\hat{\epsilon}| = 1$. The PIC electromagnetic fields then represent only the fields due to the plasma dynamics, and not the laser field. Unlike the implementation in [32], the one described here models the laser envelope in the speed-of-light frame; unlike in [33], this implementation models the wakefields explicitly. The implementation we describe here also adds a new particle push algorithm, which we show in Section 3.1 exhibits second-order convergence. The equations governing the envelope model are derived in the appendix and the references therein; here we simply restate them for convenience.

2.1. Particle push

A key innovation of envelope models is that they incorporate both the direct response of the plasma particles to the PIC wakefields and the response of the particles to the laser envelope field averaged over the time scale of a laser oscillation period. This averaged response is described by the ponderomotive force, which drives charged particles down the gradient of the laser intensity. The equation for particle momentum, including the ponderomotive force, is, from Eq. (77)

$$\frac{d\mathbf{p}}{dt} = q(\mathbf{E} + \mathbf{v} \times \mathbf{B}) - \frac{q^2}{4\bar{\gamma} m} \nabla |a|^2, \tag{4}$$

where q and m are the particle charge and mass, respectively. The parameter $\bar{\gamma}$ is the slowly-varying component of the relativistic Lorentz factor, accounting for the particle quiver motion, and is given from Eq. (59) by

$$\bar{\gamma} = \sqrt{1 + \frac{|\mathbf{p}|^2}{m^2 c^2} + \frac{q^2 |a|^2}{2 m^2 c^2}}. \tag{5}$$

The momentum $\mathbf{p}$ is the slowly-varying component of the momentum, and the corresponding velocity $\mathbf{v}$ is given by

$$\mathbf{v} = \frac{d\mathbf{x}}{dt} = \frac{\mathbf{p}}{\bar{\gamma} m} \tag{6}$$

as per Eq. (67). The normalized laser intensity $|a|^2$ is found by solving the slowly-varying wave equation for the laser envelope.

Here we describe a new algorithm implementing this update, which improves on the previous algorithm in VORPAL. That previous algorithm, described in [32], exhibited only first-order convergence as implemented in VORPAL; the new algorithm has second-order convergence, as we show in detail in Section 3.1. Another benefit of this new algorithm is that it is simpler than the previous one, requiring only linear arithmetic where the previous algorithm involved the solution of a quadratic equation and a cubic equation.

Our algorithm for the particle push is based on the relativistic Boris push algorithm, which is used in conventional PIC simulations to update particle phase space variables. The Boris algorithm can be readily adapted to include the ponderomotive effects. At first glance, this would seem quite difficult. In the Boris algorithm, to update a particle to time step $n + 1$, the momentum is first advanced from $n - 1/2$ to $n + 1/2$, with both the position and the electromagnetic fields assumed constant at their values at time n. The position is then updated from n to $n + 1$ with the momentum assumed constant at its value at time $n + 1/2$. This results in time-discretization error which is second-order in Δt. The difficulty in including the ponderomotive effects arises from the fact that $\bar{\gamma}$ must be known at the middle of the time step for the position update. This requires knowledge of $|a|^2$ at the particle position, so the particle position must be known at time $n + 1/2$. This would seem to defeat attempts to formulate a leapfrog-style algorithm.

However, a leapfrog algorithm very similar to the Boris push is possible by taking advantage of an observation about the ponderomotive force. From the equations of motion, it seems that the quantity $|a|^2$ behaves somewhat like a "potential" for the particle. This would suggest that a particle moving only under the influence of the ponderomotive force would not experience a change in some relevant "total energy" quantity. Indeed, we can attach a precise meaning to this heuristic argument by considering Eq. (82): We see that $\bar{\gamma}$ only changes as a result of an electric field or a time variation in $|a|^2$. In particular, if we can consider a to be fixed and ignore the effects of $\mathbf{E}$, then we can treat $\bar{\gamma}$ as constant.

The leapfrog algorithm can then be formulated by incorporating the change in momentum from the ponderomotive force, that is, the last term in Eq. (4), into the particle position update instead of the momentum update. In addition, consider a to be temporally located at the half-integer time steps, so that it can be considered fixed during the position update. Then, the change in $\bar{\gamma}$ from the ponderomotive force will cancel the change in $\bar{\gamma}$ from the particle's motion in the laser field, at least to second order in the time step.

We can now describe the ponderomotive particle push algorithm precisely. First, the momentum update from $n - 1/2$ to $n + 1/2$ is carried out exactly as in the Boris algorithm, except that $\bar{\gamma}$ is used in place of γ. Since the particle position is considered fixed during the momentum update, this is not problematic as long as a is known at time step n. The position update, including the ponderomotive force, proceeds as follows: We first compute $\bar{\gamma}$, which we use throughout the update as justified above. We then perform the ponderomotive force update to the momentum for half a time step, then move the particle, then perform the ponderomotive force update for the final half time step.

To describe the particle position update algorithm from time step n to $n + 1$, we denote the initial position by $\mathbf{x}|^n$, the momentum by $\mathbf{p}|_-^{n+1/2}$, and the envelope field at the middle of the time step by $a|^{n+1/2}$. We then define

$$\bar{\gamma}_0 = \frac{1}{mc}\left[\left|\mathbf{p}|_-^{n+1/2}\right|^2 + \frac{q^2\left|a|^{n+1/2}(\mathbf{x}|^n)\right|^2}{2} + m^2c^2\right]^{1/2}. \tag{7}$$

This is the $\bar{\gamma}$ we use throughout the position update. We also define the ponderomotive force for the first half of the time step,

$$\mathbf{F}|^n = \left[\nabla\left|a|^{n+1/2}\right|^2\right]_{\mathbf{x}|^n}. \tag{8}$$

We then apply the ponderomotive force to advance the momentum for the first half of the time step, obtaining its value at the middle of the time step,

$$\mathbf{p}|_0^{n+1/2} = \mathbf{p}|_-^{n+1/2} - \frac{q^2\Delta t}{8\bar{\gamma}_0 m}\mathbf{F}|^n. \tag{9}$$

We can now perform the position update:

$$\mathbf{x}|^{n+1} = \mathbf{x}|^n + \frac{\mathbf{p}|_0^{n+1/2}}{\bar{\gamma}_0 m}\Delta t. \tag{10}$$

To enable the envelope field update, detailed in the next section, we also compute the position in the middle of the position update and deposit the gridded plasma susceptibility based on that position. Finally, we apply the ponderomotive force for the second half of the step. To this end we define the relevant ponderomotive force by evaluating $\nabla|a|^2$ at position $\mathbf{x}|^{n+1}$,

$$\mathbf{F}|^{n+1} = \left[\nabla\left|a|^{n+1/2}\right|^2\right]_{\mathbf{x}|^{n+1}}. \tag{11}$$

Then we use this force to advance the momentum for the second half of the time step, so we have, for the final momentum,

$$\mathbf{p}|_+^{n+1/2} = \mathbf{p}|_0^{n+1/2} - \frac{q^2\Delta t}{8\bar{\gamma}_0 m}\mathbf{F}|^{n+1}. \tag{12}$$

This completes the update of the particle phase space variables.

2.2. Envelope field update

The evolution equation for the envelope field is derived in the Appendix, and given in Eq. (105),

$$\left[\frac{2}{\omega_0}\frac{\partial}{\partial\tau}\left(1+\frac{i}{k_0}\frac{\partial}{\partial\xi}\right)+\frac{i}{k_0^2}\nabla_\perp^2\right]a = -i\chi a. \tag{13}$$

Here ω_0 is the central frequency of the laser pulse, $k_0 = \omega_0/c$, and χ is the scalar field representing the local plasma susceptibility, given in Eq. (103).

To update the envelope field, we must discretize Eq. (13) in both time and space. We begin with the temporal discretization. For the $\partial/\partial t$ operator, we use central differencing. This requires that we use both $a|^{n+1/2}$ and $a|^{n-1/2}$ to update to $a|^{n+3/2}$, applying Eq. (13) at time $n + 1/2$ (recall that a is temporally located at half-integer time steps). In addition, for the $\nabla_\perp^2$ term, we use the Crank–Nicholson scheme, using the averaged quantity

$$\frac{a|^{n-1/2}+a|^{n+3/2}}{2} \tag{14}$$

in place of $a|^{n+1/2}$. This temporal discretization gives

$$\frac{2}{\omega_0}\left(1+\frac{i}{k_0}\frac{\partial}{\partial\xi}\right)\frac{a|^{n+3/2}-a|^{n-1/2}}{2\Delta t}+\frac{i}{k_0^2}\nabla_\perp^2\frac{a|^{n-1/2}+a|^{n+3/2}}{2} = -i\chi|^{n+1/2}a|^{n+1/2}. \tag{15}$$

We can isolate the difference $a|^{n+3/2} - a|^{n-1/2}$ to obtain

$$\frac{1}{\omega_0\Delta t}\left(1+\frac{i}{k_0}\frac{\partial}{\partial\xi}\right)\left(a|^{n+3/2}-a|^{n-1/2}\right)+\frac{i}{k_0^2}\nabla_\perp^2\frac{a|^{n+3/2}-a|^{n-1/2}}{2}+\frac{i}{k_0^2}\nabla_\perp^2 a|^{n-1/2} = -i\chi|^{n+1/2}a|^{n+1/2}, \tag{16}$$

or

$$\left[\frac{1}{\omega_0\Delta t}\left(1+\frac{i}{k_0}\frac{\partial}{\partial\xi}\right)+\frac{i}{2k_0}\nabla_\perp^2\right]\left(a|^{n+3/2}-a|^{n-1/2}\right) = -i\left(\chi|^{n+1/2}a|^{n+1/2}+\frac{1}{k_0^2}\nabla_\perp^2 a|^{n-1/2}\right). \tag{17}$$

For the spatial discretization, we use central differencing in the longitudinal direction, so

$$\left.\frac{\partial a}{\partial\xi}\right|_{j,k,l} = \frac{a|_{j+1,k,l}-a|_{j-1,k,l}}{2\Delta x}. \tag{18}$$

The transverse Laplacian takes the usual discrete form

$$\left[\nabla_\perp^2 a\right]_{j,k,l} = \frac{a|_{j,k+1,l}-2a|_{j,k,l}+a|_{j,k-1,l}}{\Delta y^2}+\frac{a|_{j,k,l+1}-2a|_{j,k,l}+a|_{j,k,l-1}}{\Delta z^2}. \tag{19}$$

To update the envelope field, then, an implicit solve of the spatially-discretized form of the operator

$$M = \frac{1}{\omega_0\Delta t}\left(1+\frac{i}{k_0}\frac{\partial}{\partial\xi}\right)+\frac{i}{2k_0}\nabla_\perp^2 \tag{20}$$

is performed to obtain $a|^{n+3/2} - a|^{n-1/2}$. This result is then added to $a|^{n-1/2}$ to compute the updated field. The AZTECOO package from the TRILINOS library [34] is used to perform the implicit solve. The matrix is expressed in its equivalent real form

$$\widehat{M} = \begin{pmatrix} \mathrm{Re}(M) & -\mathrm{Im}(M) \\ \mathrm{Im}(M) & \mathrm{Re}(M) \end{pmatrix} \tag{21}$$

so that all complex quantities can be expressed in terms of their real components. This algorithm solves the linear update equation from [33], Eq. (21), using the linear solver techniques employed for the lab-frame algorithm in [32]. In summary, the envelope model described here is similar in implementation to previous work, but with a significant change to the particle push algorithm.

3. Test problems

Before we discuss the envelope model applied to LPA cases of interest, we first describe tests conducted to ensure that the algorithm behaves as expected. These tests also quantify certain features of the algorithm's performance relative to explicit PIC.

3.1. Convergence

A key aspect of any numerical algorithm relying on gridded quantities is its ability to converge to a fixed value as grid resolution is increased. For PIC with explicit FDTD representation of the laser fields, figures of merit converge quadratically in the grid resolution. To test convergence of the envelope model, and to compare its properties to explicit FDTD, we use a simple 1D simulation. A laser pulse is launched into vacuum and propagates through a density ramp to reach a region of uniform density. The uniform density region has a density of $n = 10^{24}\ \mathrm{m}^{-3}$, and the ramp is a cosine ramp of length λ_p, where λ_p is the plasma wavelength corresponding to the uniform density n. The laser pulse has a wavelength of $\lambda = 800$ nm, a Gaussian longitudinal profile with intensity RMS of $L_{\mathrm{RMS}} = 1/k_p$ ($k_p = \omega_p/c$ is the plasma wave number), and a normalized peak intensity of $a_0 = 2$. The simulation is run for time $10\lambda_p/c$.

For the explicit FDTD simulations, the longitudinal grid spacing Δx is varied from $\lambda/16$ to $\lambda/256$. The CFL limit for stability requires $\Delta t \leqslant \Delta x/c$, and it is known that dispersion error of fields on the grid alter the group velocity for $\Delta t < \Delta x/c$ [18]. Thus, while in 1D it is possible to pick a timestep for dispersionless behavior, this is not always practical in 2 or 3D, depending on the transverse resolution required. Hence the time step Δt is set to 0.9995 of the CFL limit corresponding to the Δx for that simulation and a fixed $\Delta y = \lambda/3$ (similar to the resolution used in [4–6] to resolve the transverse wake structure). For the envelope model, Δx is varied from $\lambda_p/16$ to $\lambda_p/256$, and Δt is set to 0.9995 of the CFL limit corresponding to a fixed $\Delta y = \lambda_p/16$; fixing Δy is for consistency with the explicit simulations. In both cases four particles per cell are used with third-order interpolation and deposition.

As figures of merit for the convergence tests, we choose the amplitude and phase of the longitudinal wakefield E_x at the end of the simulation. We use a cubic spline of the gridded field to extract the peak amplitude and zero crossing location of the field. For the phase, in order to correct for the fact that simulations with different time steps will end at slightly different times, we use the quantity $k_p(x - \beta_g ct)$, where x is the computed zero crossing location, β_g is the analytic group velocity in the linear regime (see Eq. (24)) for the model used in the simulation, and t is the time at the end of the simulation. For each resolution scan, we plot errors relative to the Richardson-extrapolated value assuming quadratic convergence.

We can see in Fig. 1 that the envelope model exhibits quadratic convergence in amplitude. Indeed, the amplitude error for the envelope model with a given $\lambda_p/\Delta x$ is nearly identical to the error in explicit FDTD for the same value of $\lambda/\Delta x$. This indicates that the reduction in amplitude, due to interpolation, at the extrema of the forces is responsible for the error, as the reduction depends primarily on the ratio of grid spacing to wavelength of the driving force. In the envelope model, the driving force has wavelength λ_p, while in explicit FDTD, the force oscillates with wavelength λ. This conclusion is also supported by the fact that the errors are negative—the computed amplitudes approach their converged value from below.

The phase convergence of the envelope model, shown in Fig. 2, is more complex. At the highest resolutions, we observe quadratic convergence, with a coefficient several orders of magnitude better than explicit FDTD, for the same ratio of grid spacing to relevant wavelength; it is this ratio which characterizes how well the fields are resolved. As the resolution is reduced, we see a change in sign—since the absolute value of the error is used in the logarithmic plot, this appears as a

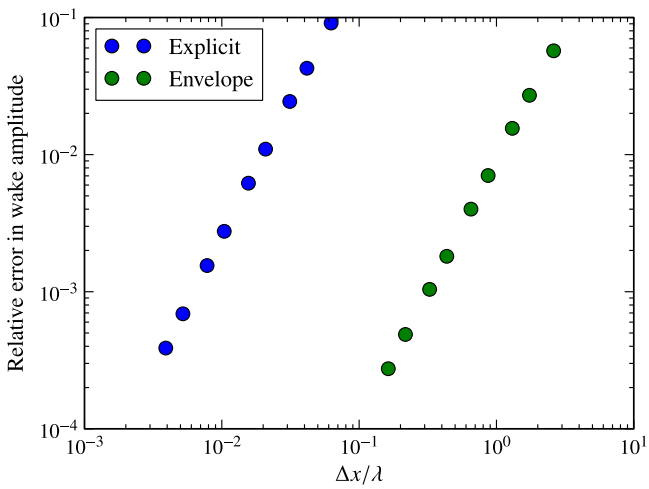

Fig. 1. Amplitude errors of explicit FDTD and the envelope model as a function of resolution.

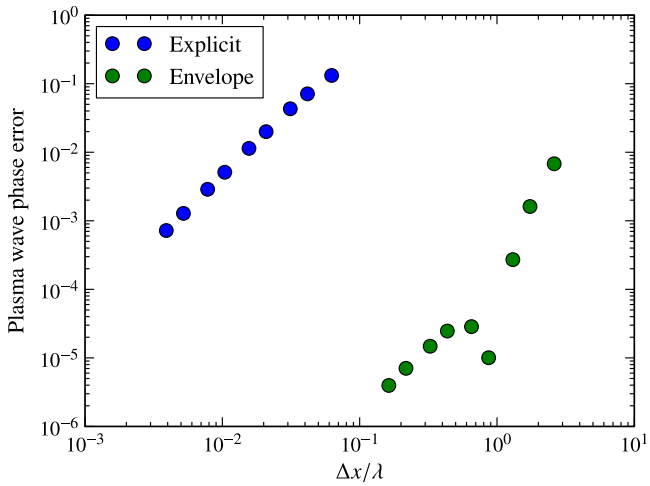

Fig. 2. Phase errors of explicit FDTD and the envelope model as a function of resolution.

cusp—followed by a different dependence. In fact, this dependence is quartic. We can subtract the quadratic dependence of the phase error computed in the Richardson extrapolation from the two highest-resolution points. The residual error after that subtraction for the remaining points is shown in Fig. 3, revealing quartic dependence.

From these results, we can conclude that for practical LPA simulations using the envelope model, in which a resolution of $\sim\lambda_p/40$ ($\sim\lambda$ for this plasma density) would be used, we would obtain a relative plasma wake amplitude error due to discretization of <1%. We would obtain a relative phase error of $<10^{-5}$. Errors on this level are unlikely to affect the qualitative results of a simulation.

3.2. Numerical group velocity and dephasing

It is well known that the Yee FDTD algorithm for evolving electromagnetic fields exhibits a numerical group velocity for electromagnetic waves that differs unphysically from the continuous case [18]. These numerical effects become more pronounced as the spatial frequency of a wave increases relative to the grid spacing. This group velocity deviation is also most pronounced for waves propagating along an axis. This is exactly the case for the laser field in an LPA simulation, which propagates along an axis, and we wish to use a grid spacing that is as large as possible while still resolving the laser oscillations. Since the laser wavelength is typically the smallest scale in the simulation, this leads to an expensive trade-off between group velocity accuracy and simulation time. While the group velocity accuracy can be improved by increasing the cell aspect ratio, there is a limit to which this is practical, due to the need to resolve the transverse wake. Because the plasma wave phase velocity is approximately equal to the laser group velocity in the limit $a_0 \ll 1$, numerical group velocity error leads to an incorrect phase offset between the plasma wave and a highly relativistic particle bunch.

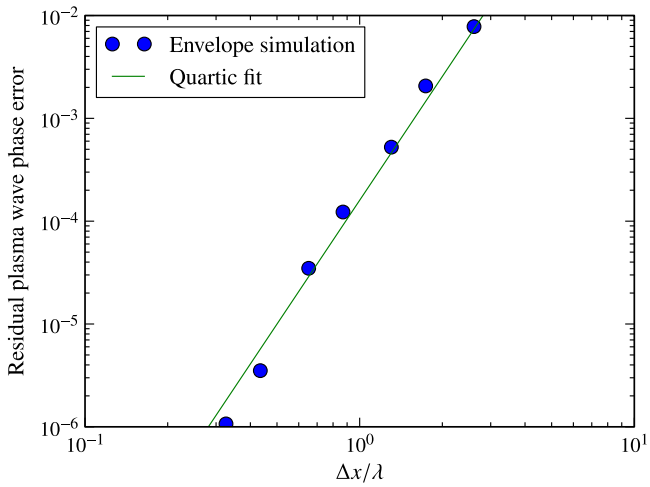

Fig. 3. Residual phase error after subtraction of the quadratic component.

Fortunately, the laser envelope model does not suffer these numerical effects, exhibiting the correct group velocity even with its coarser resolution and low aspect ratio cells. To further test the group velocity error of explicit PIC and the envelope model, we run 2D simulations of a linear ($a_0 = 10^{-3}$) laser pulse in a matched parabolic plasma channel. For linear pulses, the group velocity can be computed analytically, so we can compare both explicit and envelope simulations to theoretical values. It is known that a Gaussian laser mode with spot size w_0 is matched to a plasma channel with transverse profile $n = n_0 + r^2/\pi r_e w_0^4$ [35]. (Note that we use the notation w_0 for spot size, as per [36], rather than r_0 as in [35].) Generalizing to spot profiles which are not azimuthally symmetric, a plasma channel with transverse profile

$$n = n_0 + \frac{1}{\pi r_e}\left(\frac{y^2}{w_y^4} + \frac{z^2}{w_z^4}\right) \tag{22}$$

matches a laser mode with arbitrary spot sizes w_y and w_z in the transverse directions. The group velocity of such a mode can be characterized by the parameter k_1, given by

$$k_1^2 = {k_p^{(0)}}^2 + \frac{2}{w_y^2} + \frac{2}{w_z^2}, \tag{23}$$

where $k_p^{(0)} = \sqrt{4\pi n_0 r_e}$ is the plasma wavenumber corresponding to the background plasma density n_0. The normalized group velocity $\beta_g = v_g/c$ is then [37]

$$\beta_g = \sqrt{1 - \frac{k_1^2}{k_0^2}}. \tag{24}$$

Before we compare theoretical and simulation results, we first define an appropriate figure of merit. Since group velocities will all be fairly close to c, relative errors will be hard to detect. Instead, we choose a figure of merit that is relevant for the dephasing phenomenon, which limits the overall energy gain in an LPA stage. We therefore define the *dephasing factor* as the dimensionless parameter f_d such that a particle which propagates a distance x at the speed of light acquires a phase relative to the plasma wave of magnitude $f_d k_p x$. The plasma wave phase is given by $\phi_p = \omega_p t - k_x x$, where $k_x = \omega_p/\beta_g c$. A speed-of-light particle propagates a distance x in time x/c, and so acquires phase

$$\phi_p = \omega_p \frac{x}{c} - \frac{\omega_p}{\beta_g c} x = \left(1 - \frac{1}{\beta_g}\right) k_p x. \tag{25}$$

Since we are interested in the magnitude of the phase offset, we define the dephasing factor to be the positive number

$$f_d = \frac{1}{\beta_g} - 1. \tag{26}$$

We run tests for a range of plasma densities n_0 at the bottom of the channel. For each n_0, we let $\lambda_p = 2\pi/k_p^{(0)}$ be the corresponding plasma wavelength. Then we set the RMS length L_{RMS} of the Gaussian laser pulse intensity such that $k_p^{(0)} L_{\mathrm{RMS}} = 1$, and the transverse waist size such that $w_0 = \lambda_p$. The plasma density profile is then described by Eq. (22), with $w_y = w_0$ and

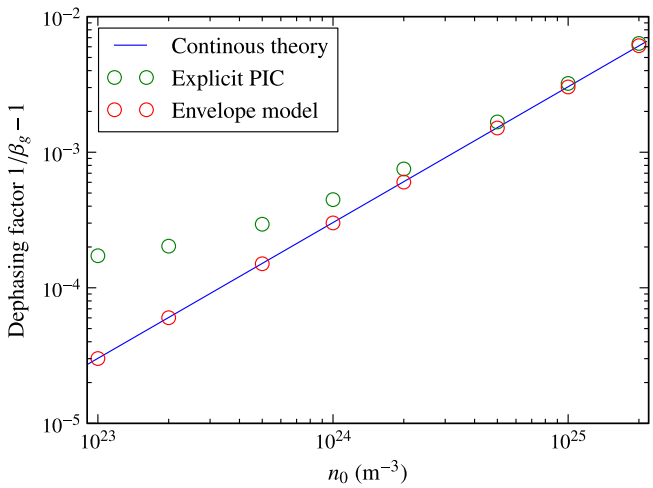

Fig. 4. The dephasing factors for explicit PIC and envelope model simulations compared to continuous theory. n_0 is the plasma density at the bottom of the plasma channel.

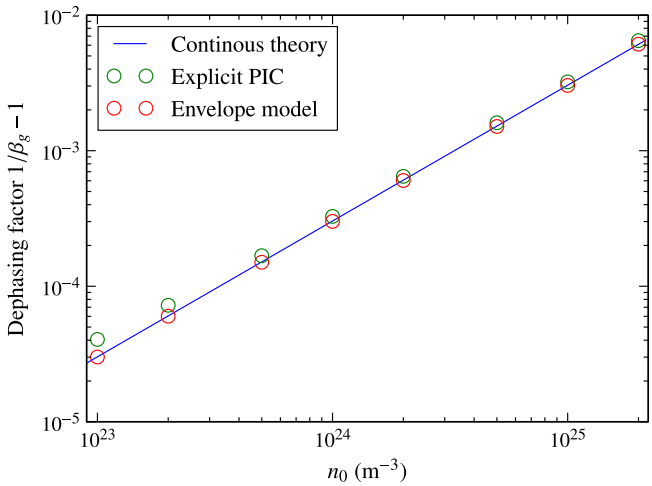

Fig. 5. The dephasing factors for explicit PIC with $\Delta y = \lambda_p/40$, the envelope model, and continuous theory.

$w_z^{-1} = 0$. We propagate the laser pulse up a cosine density ramp of length 10 μm, focusing the spot at the start of the longitudinally uniform density region. The laser pulse has a center wavelength of $\lambda = 800$ nm.

For the explicit PIC simulation, we use grid spacings of $\Delta x = \lambda/24$ and $\Delta y = \lambda/3$; for the envelope model simulations we take $\Delta x = \Delta y = \lambda_p/40$. In each case we use 1 particle per cell with 3rd-order interpolation and current deposition. The results of these tests are shown in Fig. 4. We see that while explicit PIC develops significant dephasing errors as the density is decreased, the envelope model retains the correct dephasing factor. The relative error in explicit PIC is lower at higher density because the physical dephasing is larger; the absolute errors remain the same to within a factor of 2 over the entire density range. Even at the intermediate density of $n_0 = 10^{24}$ m^{-3}, which might be used for a scaled simulation [38], explicit PIC still shows dephasing which is 50% larger than the correct value.

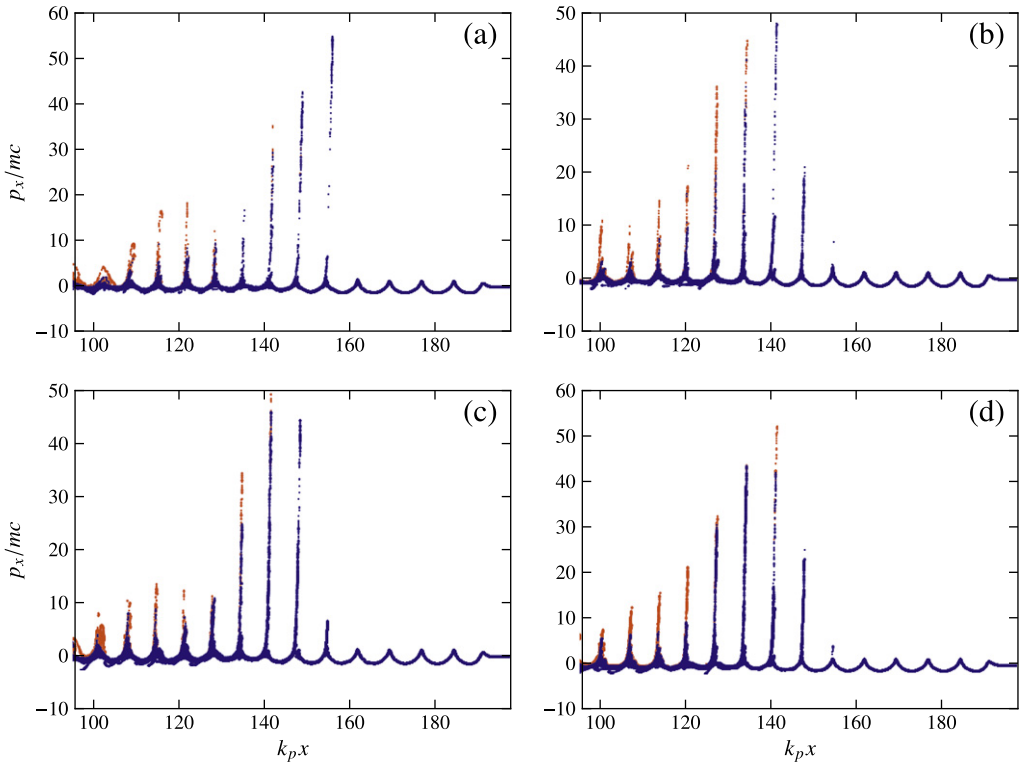

Fig. 6. Tests of resolution and particles per cell: (a) $\Delta x = \lambda_p/36$ with $N_{PPC} = 100$, (b) $\Delta x = \lambda_p/60$ with $N_{PPC} = 100$, (c) $\Delta x = \lambda_p/36$ with $N_{PPC} = 400$, and (d) $\Delta x = \lambda_p/60$ with $N_{PPC} = 400$. Particles which begin in the ramp region are shown in red; those from the uniform region in blue. (For interpretation of the references to colours in this figure legend, the reader is referred to the web version of the paper.)

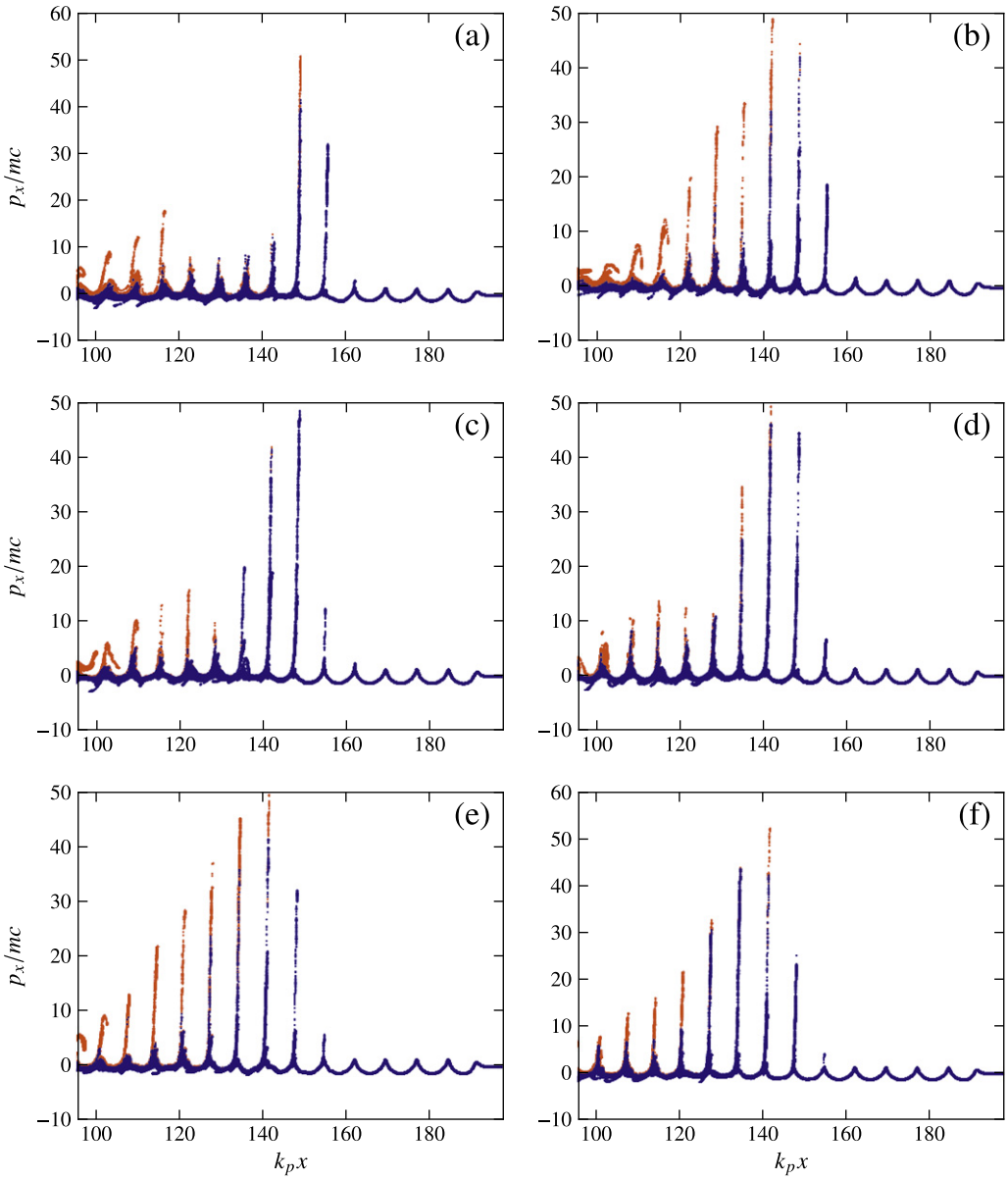

Fig. 7. Final macroparticle phase space vs. resolution for (a) $\Delta x = \lambda_p/20$, (b) $\Delta x = \lambda_p/24$, (c) $\Delta x = \lambda_p/30$, (d) $\Delta x = \lambda_p/36$, (e) $\Delta x = \lambda_p/48$, and (f) $\Delta x = \lambda_p/60$.

Attempts to use explicit, laboratory-frame FDTD to model the laser field in meter-scale simulations could alternatively increase the aspect ratio by holding $\Delta y \sim \lambda_p$ to reduces the dephasing error. Even in this case, we have found in additional simulations that it is still significantly larger than the error of the envelope model. Fig. 5 shows a comparison of the dephasing factors for the explicit case with Δy held fixed at $\lambda_p/40$, the envelope model, and continuous theory. We see that at the lowest densities, explicit FDTD still exhibits dephasing error of over 30% even in this case.

These tests show that the envelope model obtains the correct group velocity for a laser pulse in a channel, a critical quantity for LPA simulations and a distinct improvement over explicit FDTD. They also show correct propagation of laser fields at an angle, since the Gaussian pulse includes plane wave components with nonzero transverse wavevector (which would be difficult to test with a plane wave given the Cartesian nature of the grid).

3.3. Kinetics

It is known that the PIC method for simulating laser–plasma acceleration introduces error in the particle phase-space orbits due to interpolation of the fields at the locations of the particles. This has been described in detail for explicit PIC simulations in [39]. Here we examine these effects for the envelope model using 1D simulations.

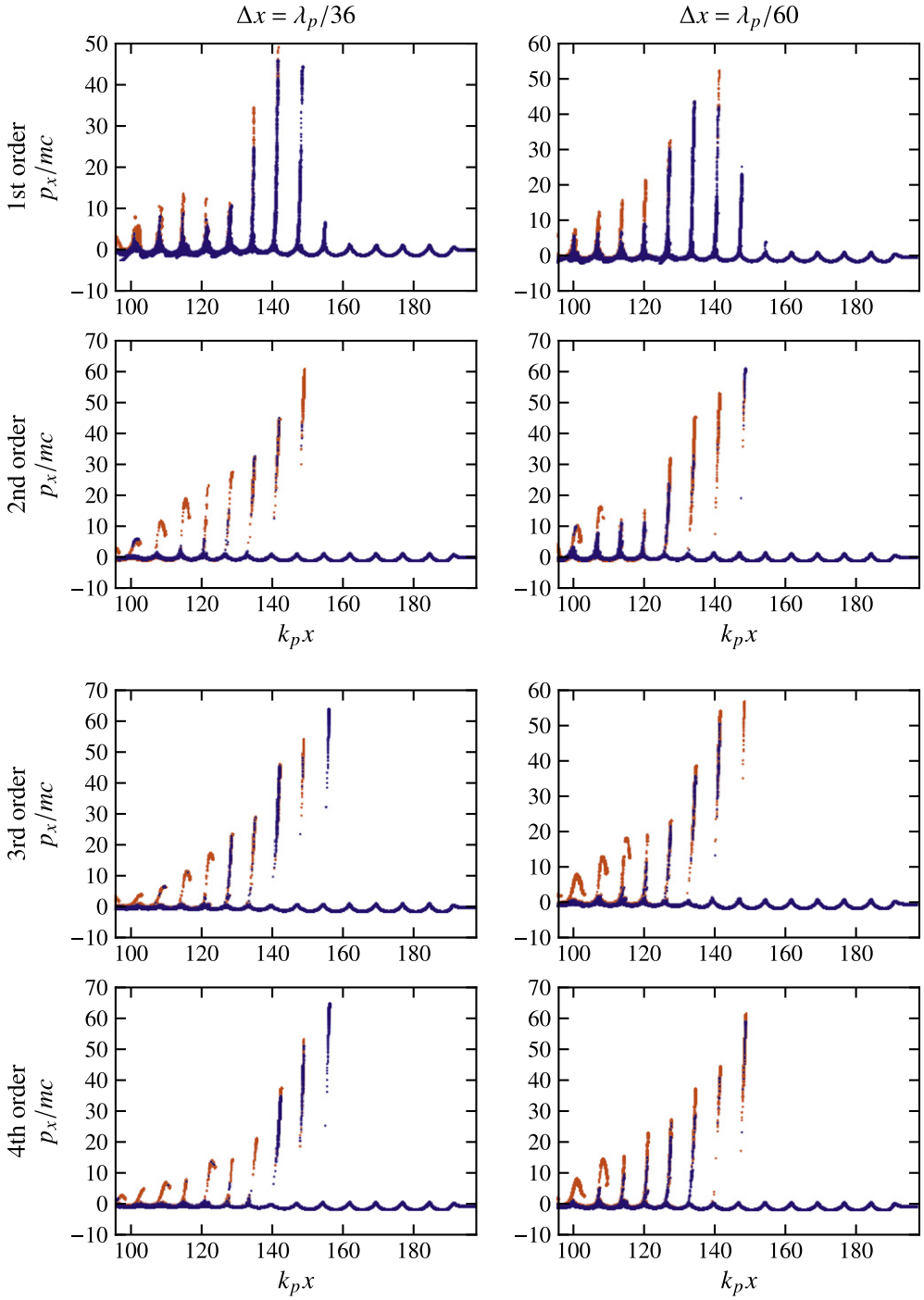

Fig. 8. Final macroparticle phase space for first- through fourth-order particles with $\Delta x = \lambda_p/36$ and $\Delta x = \lambda_p/60$ resolutions. Interpolation order varies with the row, while resolution varies with the column.

We use physical parameters identical to those used in [39]. Namely, we set the plasma density so that the ratio of wavelengths $\lambda_p/\lambda = 10$, giving a density of $n = 1.74 \times 10^{25}\ \mathrm{m}^{-3}$ for a laser wavelength of $\lambda = 800$ nm. The laser pulse starts in vacuum and propagates through a cosine ramp of length $l = 105$ μm before reaching the region of uniform plasma density. The laser pulse has a Gaussian longitudinal profile with $L_{\mathrm{RMS}} = 1/k_p$ and a normalized peak intensity of $a_0 = 2$. The simulation is run for time $31.5\lambda_p/c$, and the length of the global simulation domain is 130 μm.

We begin by looking at the basic numerical parameters of grid resolution and particles per cell for 1st-order particles. Fig. 6 shows the resulting phase space distributions for all combinations of grid spacings $\Delta x = \lambda_p/36$ and $\Delta x = \lambda_p/60$ with

particles per cell N_{PPC} = 100 and N_{PPC} = 400. We show the particles from the ramp and uniform regions using different colors because of the different physics in the two regions. The cold relativistic wave-breaking field and wakefield amplitude both vary with the plasma density, so trapping in the ramp region does not by itself indicate unphysical numerical effects. We first notice a similar but exaggerated effect of unphysical trapping relative to the explicit PIC tests reported in [39]. For instance, in the explicit tests with $\Delta x = \lambda_p/36$ and N_{PPC} = 400, injection occurs in the eighth bucket behind the laser pulse; here it occurs in the fifth. We also notice that both increasing the resolution and increasing the number of particles per cell reduces these effects. In the remainder of these tests we therefore use N_{PPC} = 400 to isolate the effects of the resolution and particle interpolation order.

Next, we consider in more detail the effect of grid resolution on unphysical trapping. Fig. 7 shows final phase space distributions for $\lambda_p/\Delta x$ = 20, 24, 30, 36, 48, and 60. We see that trapping monotonically becomes further behind the laser pulse as the resolution is increased, even at the lowest resolutions. This is in contrast to explicit PIC, in which the case for $\Delta x = \lambda/24$ showed slightly less trapping than the higher resolution. The difference could be due the convergence of the wakefield amplitude at lower resolutions in the envelope model.

Finally, we examine the effect of higher-order particles. Using-second order instead of first-order interpolation and deposition results in a much greater reduction in unphysical trapping than increasing the resolution, as noted in [39] for the explicit case. Fig. 8 shows the phase space distributions for first- through fourth-order particles for both $\Delta x = \lambda_p/36$ and $\Delta x = \lambda_p/60$ resolutions. We see that in going from first to second order with $\Delta x = \lambda_p/36$, while the injected particles in the sixth bucket have higher energy, trapping from the fifth bucket is eliminated, and there are fewer injected particles in the subsequent buckets, especially particles from the uniform plasma density region. Decreasing the grid spacing to $\lambda_p/60$ at second order eliminates injection from the fifth bucket, as well as any injection of particles from the uniform density region. However, increasing the interpolation order beyond second shows trapping again in the fifth bucket at $\Delta x = \lambda_p/36$.

These results show that while the envelope model exhibits kinetic performance slightly inferior to explicit PIC, the unphysical trapping is small enough that it will have a negligible effect on practical LPA simulations. The use of higher-order particles restricts the trapping in the uniform density region to at least five plasma wavelengths behind the laser pulse. Since the typical simulation domain is shorter than that, the moving window will shift the plasma out of the simulation before unphysical trapping develops. Together with the results on convergence and group velocity, we have shown that the envelope model behaves consistently with known physics and with high accuracy.

4. Benchmarks for full-scale simulations

Having established the performance of the envelope model algorithm in test simulations, we now demonstrate the capabilities of this model for the design of future LWFA experiments. We choose as our test case a meter-scale, quasilinear LWFA stage proposed for development at the BELLA facility at Lawrence Berkeley National Laboratory [38]. We note that this quasilinear regime uses laser intensities below the self-trapping threshold, so these stages are designed for an externally injected bunch, for instance to cascade many stages for a high-energy collider [7]. An advantage of the quasilinear regime is that acceleration and focusing of a positron beam can be carried out in a manner nearly symmetric to that of an electron beam.

For this case, we take the plasma density at the bottom of the channel to be $n_0 = 10^{23}\ \mathrm{m}^{-3}$, which gives a plasma wavelength of λ_p = 106 μm. We can compute the linear dephasing length associated with this density using Eq. (25). The dephasing length L_d is the distance a particle propagates in which the plasma wave phase seen by the particle slips by π, so

$$\left(\frac{1}{\beta_g} - 1\right) k_p L_d = \pi, \tag{27}$$

where $k_p = 2\pi/\lambda_p$; this gives

$$L_d = \frac{\pi}{(1/\beta_g - 1)k_p} = \frac{\lambda_p}{2(1/\beta_g - 1)}. \tag{28}$$

Using Eq. (24) in the limit $k_1 \ll k_0$ gives $1/\beta_g - 1 = k_1^2/2k_0^2$, where k_1 is given by Eq. (23). Thus

$$L_d = \frac{\lambda_p}{k_1^2/k_0^2} = \frac{k_0^2\lambda_p}{k_p^2 + 2/w_y^2 + 2/w_z^2} = \frac{k_0^2\lambda_p}{k_p^2\left[1 + 2/(k_p w_y)^2 + 2/(k_p w_z)^2\right]} = \frac{\lambda_p^3}{\lambda^2}\left[1 + \frac{2}{(k_p w_y)^2} + \frac{2}{(k_p w_z)^2}\right]^{-1}. \tag{29}$$

For our parameters, this gives L_d = 1.97 m. To balance the competing goals of having a long depletion length by avoiding depletion into the transverse wake (which motivates a large spot size), with avoiding self-focusing (which requires a small spot size), we choose $k_p w_0$ = 5.3, as in [40]. In order for the particle bunch to remain in the focusing phase of the transverse wake, we choose a shorter plasma length of $L = \lambda_p^3/2\lambda^2 = 920$ mm. Finally, we choose an RMS (intensity) laser pulse length given by $k_p L_{RMS}$ = 1 and a normalized peak intensity of a_0 = 1, based on the studies in [38,40].

As we demonstrate the envelope model for these experimental parameters, we wish to benchmark against explicit FDTD simulations of the same parameters. Unfortunately, performing such meter-scale simulations with explicit, laboratory-frame FDTD is intractable, even in 2D. We therefore compare the envelope model to explicit FDTD for scaled simulations, in which the plasma density is increased to $10^{25}\ \mathrm{m}^{-3}$ for the simulation, and quantities in the simulation results are then scaled

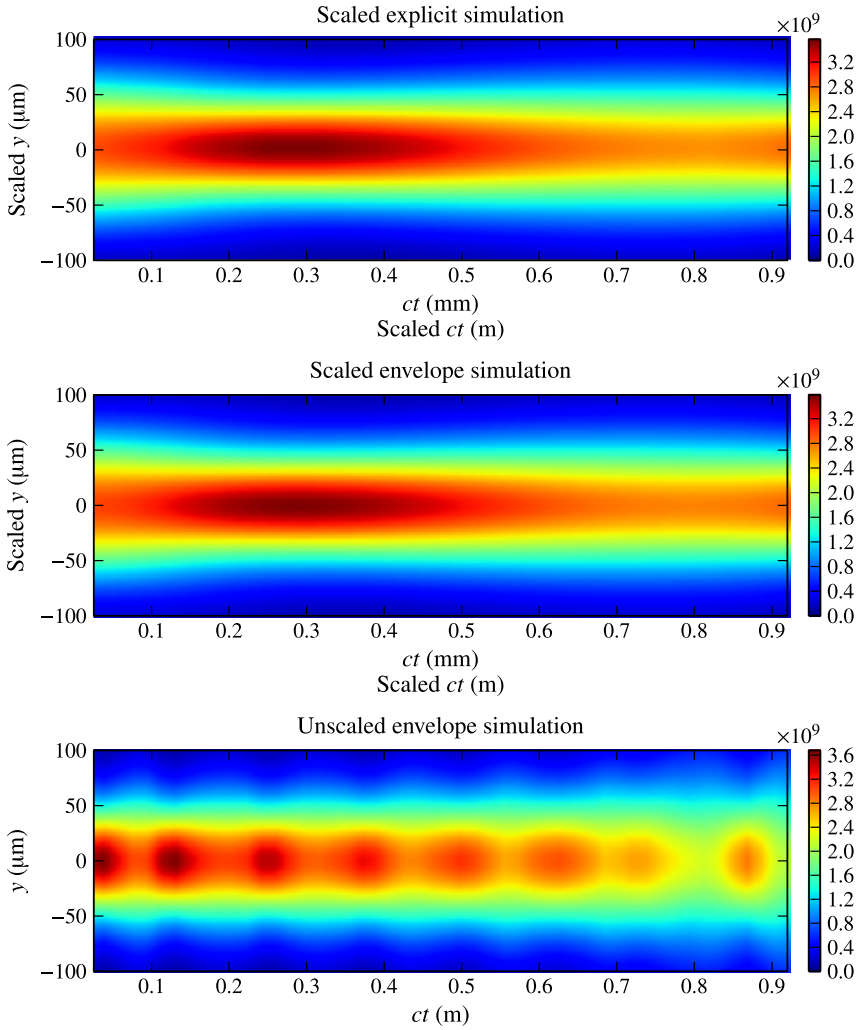

Fig. 9. Fluence profiles of the laser pulse, in J/m^2. Agreement between explicit and envelope scaled simulations can be seen, and more rapid self-focusing oscillations are visible in the unscaled case.

appropriately to the meter-scale case [38]. In such simulations, the laser pulse length and spot size are scaled proportionally to λ_p. The dephasing length scales as λ_p^3, and the acceleration and laser depletion lengths were shown to scale by that amount; and since the wakefield strength scales as λ_p^{-1}, total energy gain by a particle bunch was shown to scale as λ_p^2. The normalized laser intensity a_0 is held constant. We also compare the explicit and envelope scaled simulations to an unscaled simulation using the envelope model. This will demonstrate any physical differences between the scaled and unscaled parameters. It was shown in [38,40] that the wake structure is preserved by scaling in this manner, but that the ratios of laser and electron beam focusing oscillation wavelength to the dephasing length were not. Thus the envelope model can be used to accurately model and hence mitigate undesired effects of focusing oscillations.

We run each simulation in 2D. For the explicit simulation, we choose grid spacings of $\Delta x = 33$ nm and $\Delta y = 134$ nm, global simulation domain sizes of $L_x = 3.5\lambda_p = 37.0$ μm and $L_y = 59.9$ μm for grid sizes of $N_x = 1108$ and $N_y = 448$; this includes 24 cells along each transverse edge for a perfectly-matched layer (PML) absorbing boundary [18, Chapter 7]. These parameters are similar to those in [38], and they have been shown to be well-converged [40]. In the envelope scaled simulation, the laser oscillations need not be resolved, so we use $\Delta x = 210$ nm, $\Delta y = 264$ nm (the smaller Δx is used to better resolve the laser envelope), $L_x = 37.0$ μm, and $L_y = 66.5$ μm, for a grid size of $N_x \times N_y = 176 \times 252$. (The difference in L_y is due to the fact that the number of transverse cells in each PML region is fixed at 24, while the transverse grid spacing in the envelope simulation is larger.) For the envelope unscaled simulation, since the density for the scaled simulations is increased by a factor of 100, λ_p is 10 times greater than the scaled case. The grid spacings and global domain sizes are therefore larger by that factor relative to the scaled simulation, and the number of grid points in each dimension remain the same. This reveals the key advantage of the envelope model: Lower densities are accessible since the longer plasma wavelength can be simulated with a proportionally larger grid spacing. In addition, since the time step is proportional to the grid spacings via the Courant condition, Δt also

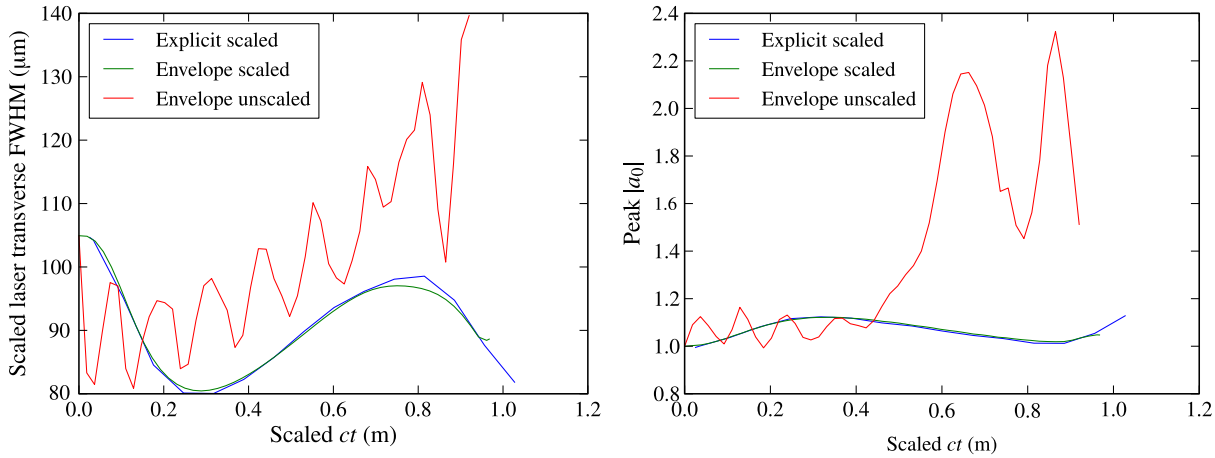

Fig. 10. Left: Transverse spot size of the laser pulse, measured as the full width at half maximum (FWHM) of the fluence. Right: The peak normalized laser field intensity.

scales as λ_p. Since the propagation distance scales as λ_p^3, the number of time steps scales as λ_p^2 for the envelope model; since no such time step scaling is available with explicit FDTD, the number of steps scales as λ_p^3 for that algorithm.

We first compare the evolution of the laser pulse. We can examine the transverse profiles of the laser pulse by plotting the fluence as a function of transverse position y and approximate propagation distance ct. This is shown in Fig. 9. From this Figure, we first note the excellent agreement between the explicit and envelope scaled simulations, indicating that the envelope update remains faithful to the laser evolution given by the Maxwell equations. We also see that in the unscaled case, the transverse spot size oscillations in the laser profile are much more rapid. This is not surprising, since it is known that scaled simulations do not correctly model the period of such oscillations. Because of relativistic self-focusing, the laser pulse is not perfectly matched to the plasma channel; the plasma channel radius was modified from the linear case to compensate for self-focusing, but the compensation was not perfect. We therefore expect some focusing of the laser pulse and a mismatched spot size oscillation. In the low power limit, a mismatched laser pulse will oscillate in a channel with a period πx_R, where $x_R = \pi w_0^2/\lambda$ is the matched Rayleigh length [37]. This length therefore scales with plasma density as λ_p^2, but the propagation distance scales with λ_p^3. Scaling therefore extends the focusing length relative to scaled propagation distance, as seen in Fig. 9.

Looking more closely at the evolution of the laser pulse reveals some limitations of the unscaled envelope model while still showing excellent agreement with explicit FDTD for scaled simulations. To examine this further, we consider the evolution of the transverse spot size of the laser pulse as well as the peak field intensity. These are shown in Fig. 10. In the left plot in the figure, we see, as in the fluence profile plot, the expected more rapid oscillations in the unscaled case, while the envelope and explicit scaled simulations agree quite well. The same is true for the peak field intensity, until about 45 cm of propagation. At that point the peak intensity in the unscaled simulation doubles from its original value, which oscillated

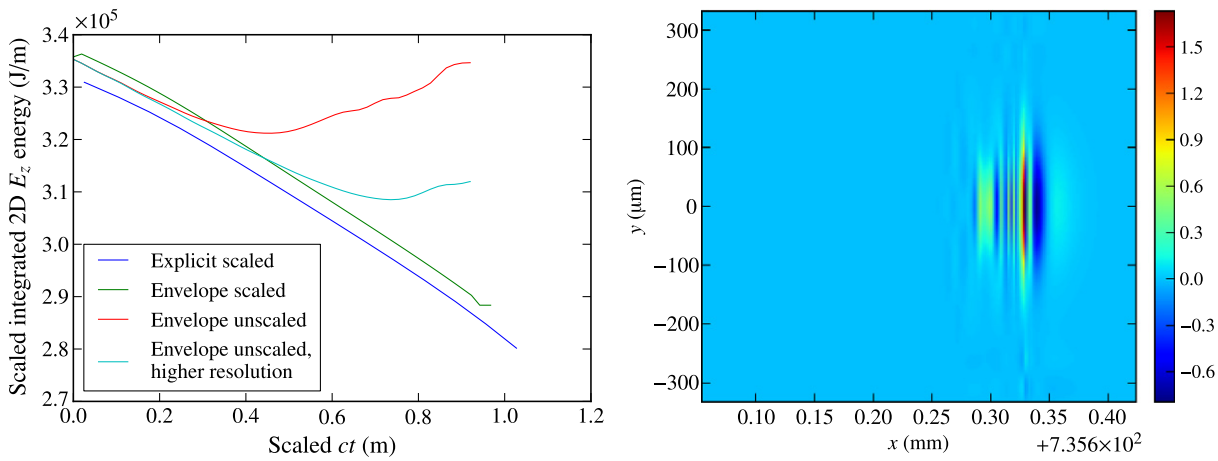

Fig. 11. Left: Total energy in the laser pulse. Right: The real part of the normalized laser amplitude envelope derived from the vector potential, given by Re(qa/mc), at 736 mm of propagation in the unscaled envelope simulation. This shows the high-frequency oscillations developing in the envelope field. These are unresolved by the grid, causing the unphysical behavior shown in the left plot.

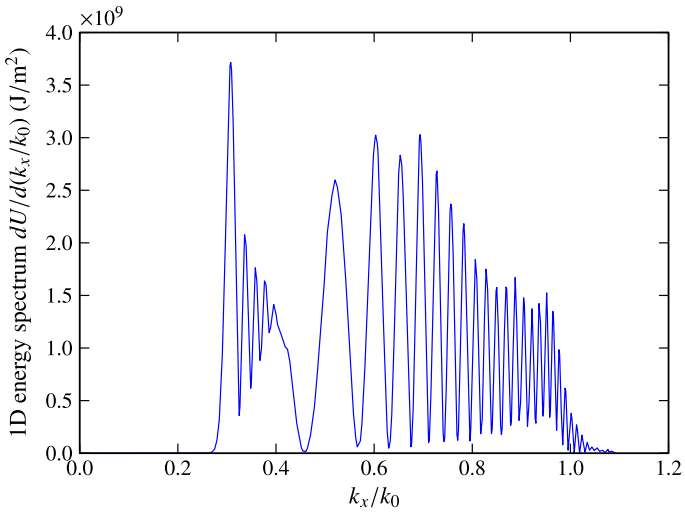

Fig. 12. The energy spectrum, as a function of spatial frequency normalized to k_0, of a laser pulse after 2.1 m of propagation through a plasma with density 10^{23} m^{-3}. The laser pulse evolution was computed using a 1D explicit simulation.

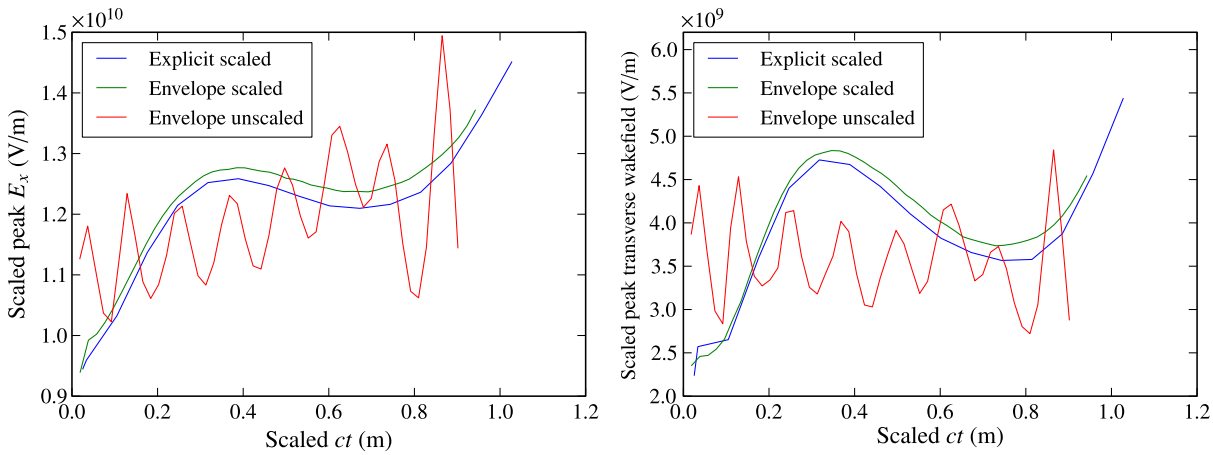

Fig. 13. Left: The peak longitudinal wakefield. Right: The peak transverse wakefield.

between $a_0 = 1.0$ and $a_0 = 1.2$. Furthermore, this increase is not simply due to self-focusing, as it is not accompanied by a similar reduction in transverse spot size. The unphysical nature of this evolution is clearly shown in the left plot of Fig. 11. We see that unlike in the scaled case, in the unscaled envelope simulation, the total laser energy actually starts to increase after about 45 cm of propagation. There is no physical mechanism which should cause this. Instead, the unphysical evolution can be traced to lack of resolution of the laser envelope field. In the right plot of Fig. 11, the real part of the normalized vector potential laser envelope, namely $\mathrm{Re}(qa/mc)$, is plotted for the unscaled envelope simulation at 736 mm of propagation. We can see that fast oscillations in the envelope have developed; given that there are only 175 grid points longitudinally, these oscillations are not well resolved.

This under-resolution of the envelope fields is caused by a shift in the spectrum of the laser pulse. By using the envelope field as defined in Eq. (51) along with a coarse grid, we have assumed that the longitudinal spatial frequency spectrum, as well as the temporal spectrum, occupies a narrow band around k_0. While this assumption holds early on in the pulse propagation, redshifting caused by laser depletion broadens the spectrum beyond what is resolved on the grid. Theory and simulations [41] show that the mean pulse frequency scales with the characteristic laser depletion length L_{pd}. Thus $d\omega/dx \sim \omega_0/L_{\mathrm{pd}}$, where the total laser pulse energy U also evolves as $dU/dx \sim U_0/L_{\mathrm{pd}}$. Here ω_0 and U_0 are the initial laser central frequency and pulse energy, respectively. Simply put, significant frequency shifts $\Delta\omega \sim \omega_0$ occur after a depletion length. For $a_0 \sim 1$, $L_{\mathrm{pd}} \sim \lambda_p^3/\lambda^2 \sim L_d$, so we expect a significant frequency shift to occur within a single stage. A given longitudinal grid spacing Δx allows a resolved bandwidth proportional to Δx^{-1}. Therefore this problem is more severe for the unscaled case than the scaled case, since $\Delta x/\lambda_p$ is held constant, and hence $\Delta x/\lambda_0$ is larger, resulting in a narrower bandwidth limit. We can see this dramatically in Fig. 12, in which the spectrum of a laser pulse after long distance propagation, modeled in a 1D explicit simulation, is plotted. We can

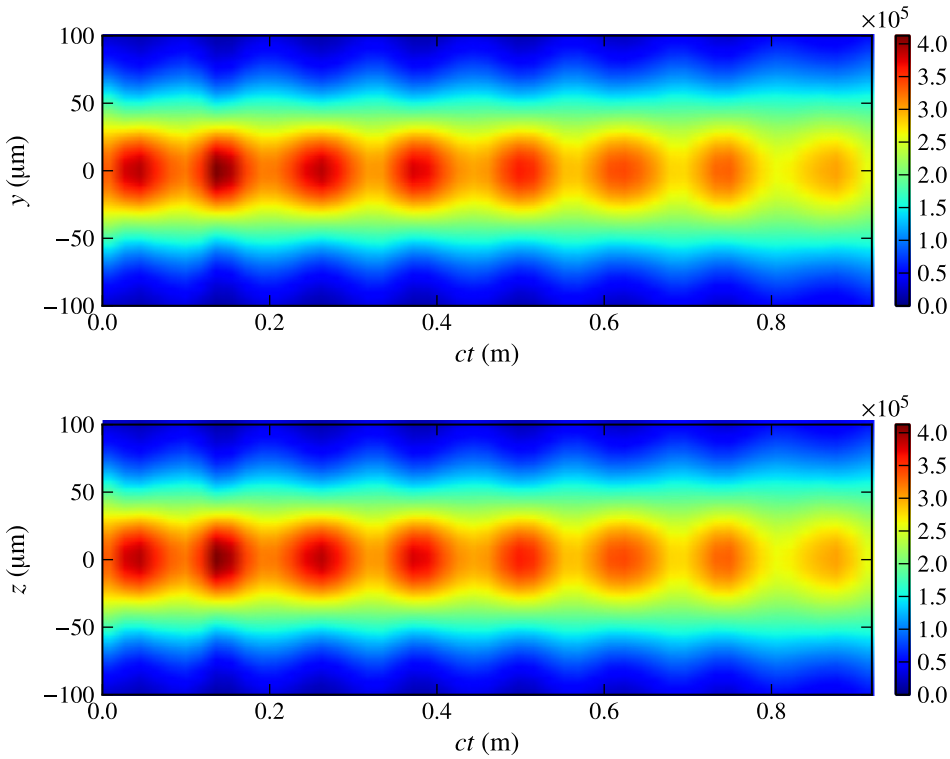

Fig. 14. Fluence profiles of the laser pulse from the 3D simulation. The fluence is integrated in z (top) and y (bottom), to give the fluence dependence on y and z, respectively. The units are J/m.

demonstrate this phenomenon of insufficient longitudinal resolution directly, by running the unscaled envelope simulation with twice the longitudinal resolution, using $\Delta x = 105$ μm. This is shown in the light blue[1] curve in the left plot of Fig. 11. We can see that the unphysical growth in laser energy is delayed and much less pronounced, consistent with the hypothesis that longitudinal under-resolution causes the unphysical behavior. While the longitudinal resolution could be increased to better capture these depletion effects, the envelope model derives its speedup over explicit PIC primarily from lower longitudinal resolution. The user therefore has a trade-off between speed and resolution of depletion effects. We can quantify this trade-off by noting that the simulation with doubled resolution runs 67% longer (0.75 m vs. 0.45 m) before the total laser energy starts to increase. This comes at a cost of a factor of 3.9 in speed in these simulations.

Finally, we compare the wakefields for the three types of simulations. The peak longitudinal and transverse wakefield values are plotted in Fig. 13. Again we see good agreement between the two scaled simulations. Direct comparison of the unscaled envelope simulation with explicit FDTD is not possible because of the extraordinary computational requirements of an explicit simulation with those parameters. However, we can see that wakefield results in the unscaled case are physically reasonable. Despite the unphysical behavior in the laser envelope documented above, the wakefield values in the unscaled simulation do not deviate by more than ~10% from either the values in the scaled simulations or the values early on in the unscaled simulation, averaging over the self-focusing oscillations. As noted above, the self-focusing oscillations themselves behave reasonably. Since the particle beam responds to the wakefields, and not directly to the laser, this, together with the good agreement in the scaled case, provides some confidence that a full-scale simulation with the envelope model which includes an accelerated bunch will produce reasonably accurate values for the particle beam parameters, even late in the simulation. In the future, we expect to benchmark the envelope model in this unscaled case against other advanced techniques for performing this simulation, such as the boosted-frame methods, as those techniques develop further.

Now that a comparison of the physical parameters is complete, we describe the relative speed of the envelope model. To do so, 2D simulations are run with both explicit FDTD and the envelope model for identical physical parameters relevant for a meter-scale LWFA stage. Specifically, the physical parameters used are the same as those used in the unscaled case of the scaled/unscaled comparison described above. For the explicit simulation, grid spacings of $\Delta x = \lambda/32$ and $\Delta y = \lambda/3$ are used, yielding a grid size of 10083×2028. For the envelope model, grid spacings of $\lambda_p/32$ in each direction are used, which give a grid size of 77×194. Third-order particles are used in each case, and each simulation is run for 100 time steps with the global domain completely filled with plasma particles. The explicit simulation completes the 100 steps in 17.7 s on 320 cores,

[1] For interpretation of color in Figs. 1-14, the reader is referred to the web version of this article.

and the envelope model in 5.33 s on 2 cores, in both cases on the Franklin supercomputer at NERSC. The time step is 8.26×10^{-17} s for the explicit simulation and 7.74×10^{-15} s for the envelope model, so the envelope model requires fewer time steps than explicit PIC for the same propagation distance. These results yield a speedup factor of 5.0×10^4 of the envelope model over explicit FDTD. We can estimate the speedup factor in 3D by multiplying the 2D result by the ratio of explicit to envelope $N_z = N_y$, giving an estimated speedup of 5.2×10^5.

A full meter-scale envelope simulation was run in 3D, with parameters identical to the unscaled 2D case described above. The run required 10 days on 144 cores; because of the small grid size, running with greater parallelization resulted in diminishing returns on runtime, so it is unlikely that meter-scale, 3D simulations can be completed with envelope model in less than several days of runtime. Still, such a simulation only requires a moderate-size cluster rather than a supercomputer, and represents a vast improvement over explicit FDTD, for which the simulation would be entirely intractable. One could use greater parallelization to increase the longitudinal resolution, delaying the onset of unresolved laser oscillations. This allows 3D simulations of next-generation experiments on current computers. Fluence profiles of the 3D laser pulse in each transverse direction are shown in Fig. 14.

5. Conclusion

We have described in detail the implementation of a reduced model for laser–plasma accelerator simulations. This implementation includes a new ponderomotive particle push algorithm, which was shown, as implemented, to exhibit at least second-order convergence, with accuracy equal to or better than explicit PIC even with much lower resolution. The envelope model also reproduces the theoretical laser group velocity in a plasma channel—a critical parameter for simulations of LPA stages—much more faithfully than explicit PIC. At the same time, the envelope model does not suffer from numerical kinetic effects significant enough to cause unphysical trapping in typical LPA simulations.

Detailed comparisons were performed among scaled explicit, scaled envelope, and unscaled envelope simulations. We found excellent agreement between the scaled simulation, and good agreement of the wake field strength between the scaled and unscaled simulations, given the physical difference in self-focusing oscillations. We measured a speedup factor of 50,000 over explicit PIC in 2D for parameters relevant to a meter-scale LPA stage, yielding an estimated speedup factor of over 500,000 for 3D simulations. The limitation of the envelope model is in its ability to resolve the spectral broadening that occurs after long propagation distances while maintaining this low computational cost. Still, our investigations have shown that the laser envelope model provides a tool capable of performing full 3D simulations of meter-scale LPA stages. It is complementary to, and can provide benchmarks for, other models under development such as the boosted-frame method. These tools will take on ever-increasing importance as longer LPA stages are explored on a path to a high-energy collider.

Acknowledgments

This work was supported by US Department of Energy, Office of Science Grants DE-FC02-07ER41499 (SciDAC), DE-SC0000840 (SBIR), and DE-AC02-05CH11231 (LBNL), and by Tech-X Corporation. This research used resources of the National Energy Research Scientific Computing Center, which is supported by the Office of Science of the US Department of Energy under Contract No. DE-AC02-05CH11231. In addition, we acknowledge additional support for VORPAL development from the offices of Fusion Energy Sciences, High Energy Physics, and Nuclear Physics and the SciDAC program of the Department of Energy Office of Science, the Air Force Office of Scientific Research, the Joint Technology Office, and Office of the Secretary of Defense, and the SBIR programs of the Department of Energy and Department of Defense.

The authors thank J.R. Cary, D. Gordon, W.P. Leemans, C.B. Schroeder, B. Shadwick, and J.-L. Vay for helpful discussions and advice. We also acknowledge members of the VORPAL development team: T. Austin, G.I. Bell, R.S. Busby, J. Carlsson, J.R. Cary, M. Carey, D.A. Dimitrov, A. Hakim, J. Loverich, S. Mahalingam, P.J. Mullowney, C. Nieter, C. Roark, S.W. Sides, N.D. Sizemore, D.N. Smithe, P.H. Stoltz, S.A. Veitzer, D.J. Wade-Stein, G.R. Werner, M. Wrobel, N. Xiang, and C.D. Zhou.

Appendix A. Theoretical background

In this appendix we derive the key theoretical results enabling the envelope model, namely Eqs. (4)–(6) and (13). While none of these results are original (see the references for previous derivations), we provide a rigorous treatment here which may be clearer in the context of the envelope algorithm.

A.1. Relativistic ponderomotive force

As described in Section 2.1, the response of the particles to the laser field is described by the ponderomotive force. Such motion can be solved exactly in the case of a plane wave whose amplitude depends only on $x - ct$, using the Hamilton principal function [42] or the cold fluid equations [3,43]. In the case of a laser pulse whose amplitude can vary slowly in all space-time dimensions, the ponderomotive force has been derived by introducing derivatives over fast and slow space and time scales into the equations of motion [23,44]. Other derivations have used a Lagrangian technique [45] and Newtonian perturbation theory [46]. Here we derive the ponderomotive force from Hamiltonian perturbation theory.

A.1.1. Electromagnetic Hamiltonian in the speed-of-light frame

The first step in deriving the relativistic ponderomotive force is to transform to a Galilean frame co-propagating with the laser field at the speed of light. This will serve to make the Hamiltonian time-independent in the case of a plane wave. We begin with the relativistic Hamiltonian for a particle in an electromagnetic field:

$$H = c(|\mathbf{P} - q\mathbf{A}|^2 + m^2c^2)^{1/2} + q\Phi. \tag{30}$$

Here $\mathbf{P}$ is the canonical momentum given by $\mathbf{P} = \mathbf{p} + q\mathbf{A}$, where $\mathbf{p}$ is the particle's physical momentum. To transform to the speed-of-light frame we use a canonical transformation generated by the function

$$F(\mathbf{x}, \mathbf{P}', t) = (x - ct)P'_x + \mathbf{x}_\perp \cdot \mathbf{P}'_\perp. \tag{31}$$

This transformation gives

$$\mathbf{P} = \frac{\partial F}{\partial \mathbf{x}} = \mathbf{P}', \quad \mathbf{x}' = \frac{\partial F}{\partial \mathbf{P}'} = \hat{\mathbf{x}}(x - ct) + \mathbf{x}_\perp, \tag{32}$$

i.e. all coordinates remain unchanged except for the x coordinate; we denote the new x coordinate by $\xi = x - ct$. The transformed Hamiltonian is then given by [47]

$$H' = H + \frac{\partial F}{\partial t} = c(|\mathbf{P} - q\mathbf{A}|^2 + m^2c^2)^{1/2} - cP_x + q\Phi. \tag{33}$$

We now have a coordinate transformation $(t,x) \mapsto (\tau, \xi)$, with $\tau = t$. The inverse transformation is given by $t = \tau$, $x = \xi + c\tau$. Partial derivatives then transform in the following way:

$$\frac{\partial}{\partial \tau} = \frac{\partial t}{\partial \tau}\frac{\partial}{\partial t} + \frac{\partial x}{\partial \tau}\frac{\partial}{\partial x} = \frac{\partial}{\partial t} + c\frac{\partial}{\partial x}, \quad \frac{\partial}{\partial \xi} = \frac{\partial t}{\partial \xi}\frac{\partial}{\partial t} + \frac{\partial x}{\partial \xi}\frac{\partial}{\partial x} = \frac{\partial}{\partial x}, \tag{34}$$

$$\frac{\partial}{\partial t} = \frac{\partial \tau}{\partial t}\frac{\partial}{\partial \tau} + \frac{\partial \xi}{\partial t}\frac{\partial}{\partial \xi} = \frac{\partial}{\partial \tau} - c\frac{\partial}{\partial \xi}, \quad \frac{\partial}{\partial x} = \frac{\partial \tau}{\partial x}\frac{\partial}{\partial \tau} + \frac{\partial \xi}{\partial x}\frac{\partial}{\partial \xi} = \frac{\partial}{\partial \xi}. \tag{35}$$

A.1.2. Change of independent variable

We will be examining a case where the vector potential experiences fast oscillations in the ξ coordinate, so it will be useful to have use ξ, rather than τ, as the independent variable in the Hamiltonian formalism. Converting between derivatives with respect to τ and those with respect to ξ is straightforward, since causality requires $d\xi/d\tau < 0$ everywhere. To perform the transformation, we will use P_x as the Hamiltonian quantity, so we first need to express P_x in terms of H', the phase space coordinates, and τ. We have that

$$(H' + cP_x - q\Phi)^2 = c^2(|\mathbf{P} - q\mathbf{A}|^2 + m^2c^2), \tag{36}$$

which gives

$$|\mathbf{P}_\perp - q\mathbf{A}_\perp|^2 + m^2c^2 = \left(\frac{H'}{c} + P_x - q\frac{\Phi}{c}\right)^2 - (P_x - qA_x)^2 = \left(\frac{H'}{c} + 2P_x - q\frac{\Phi}{c} - qA_x\right)\left(\frac{H'}{c} - q\frac{\Phi}{c} + qA_x\right). \tag{37}$$

Then

$$\frac{H'}{c} + 2P_x - q\frac{\Phi}{c} - qA_x = \frac{|\mathbf{P}_\perp - q\mathbf{A}_\perp|^2 + m^2c^2}{H'/c - q\Phi/c + qA_x}, \tag{38}$$

so we have

$$P_x = \frac{1}{2}\left(\frac{|\mathbf{P}_\perp - q\mathbf{A}_\perp|^2 + m^2c^2}{H'/c - q\Phi/c + qA_x} - \frac{H'}{c} + q\frac{\Phi}{c} + qA_x\right). \tag{39}$$

To find the Hamilton equations for this system, we need to compute the partial derivatives of P_x. We let ψ be one of the variables $\mathbf{P}_\perp$, ξ, $\mathbf{x}_\perp$, or τ—that is, any phase space or independent variable other than H' and P_x. Holding fixed the other variables listed above, we define a function $f : \mathbb{R}^2 \to \mathbb{R}^2$ by

$$f(P_x, \psi) = (H'(P_x, \psi, \ldots), \psi). \tag{40}$$

Its Jacobian derivative is

$$Df = \begin{pmatrix} \partial H'/\partial P_x & \partial H'/\partial \psi \\ 0 & 1 \end{pmatrix}, \tag{41}$$

so the Jacobian of its inverse is given by

$$D(f^{-1}) = \begin{pmatrix} \partial P_x/\partial H' & \partial P_x/\partial \psi \\ 0 & 1 \end{pmatrix} = \begin{pmatrix} \partial H'/\partial P_x & \partial H'/\partial \psi \\ 0 & 1 \end{pmatrix}^{-1} = \frac{1}{\partial H'/\partial P_x} \begin{pmatrix} 1 & -\partial H'/\partial \psi \\ 0 & \partial H'/\partial P_x \end{pmatrix}. \tag{42}$$

This general relation yields

$$\frac{\partial P_x}{\partial H'} = \frac{1}{\partial H'/\partial P_x} = \frac{1}{d\xi/d\tau} = \frac{d\tau}{d\xi}, \tag{43}$$

and for ψ,

$$\frac{\partial P_x}{\partial \psi} = -\frac{\partial H'/\partial \psi}{\partial H'/\partial P_x} = \frac{d\tau}{d\xi}\left(-\frac{\partial H'}{\partial \psi}\right). \tag{44}$$

Then we have

$$\frac{\partial P_x}{\partial \mathbf{P}_\perp} = \frac{d\tau}{d\xi}\left(-\frac{\partial H'}{\partial \mathbf{P}_\perp}\right) = \frac{d\tau}{d\xi}\left(-\frac{d\mathbf{x}_\perp}{d\tau}\right) = -\frac{d\mathbf{x}_\perp}{d\xi}, \tag{45}$$

$$\frac{\partial P_x}{\partial \tau} = \frac{d\tau}{d\xi}\left(-\frac{\partial H'}{\partial \tau}\right) = \frac{d\tau}{d\xi}\left(-\frac{dH'}{d\tau}\right) = -\frac{dH'}{d\xi}, \tag{46}$$

$$\frac{\partial P_x}{\partial \mathbf{x}_\perp} = \frac{d\tau}{d\xi}\left(-\frac{\partial H'}{\partial \mathbf{x}_\perp}\right) = \frac{d\tau}{d\xi}\frac{d\mathbf{P}_\perp}{d\tau} = \frac{d\mathbf{P}_\perp}{d\xi}. \tag{47}$$

Together these relations show that $-P_x$ is a Hamiltonian function of the phase space conjugate variable pairs $(-\tau, H')$, (y, P_y), and (z, P_z). It follows that $dP_x/d\xi = \partial P_x/\partial \xi$. To summarize, then, we have as our Hamiltonian equations

$$\frac{d\tau}{d\xi} = \frac{\partial P_x}{\partial H'}, \quad \frac{d\mathbf{x}_\perp}{d\xi} = -\frac{\partial P_x}{\partial \mathbf{P}_\perp}, \tag{48}$$

$$\frac{dH'}{d\xi} = -\frac{\partial P_x}{\partial \tau}, \quad \frac{d\mathbf{P}}{d\xi} = \frac{\partial P_x}{\partial \mathbf{x}'}. \tag{49}$$

Note that the second of the equations in (49) is extended to include the longitudinal component as well as the transverse components.

A.1.3. Exact solution for a plane wave

We consider the case of a plane wave traveling in the $+x$ direction and consisting of a fast oscillation at angular frequency ω_0 modulated by a slowly-varying envelope. In the Coulomb gauge, the vector potential is transverse and $\Phi = 0$. We can then write $\mathbf{A}(\mathbf{x}) = \mathrm{Re}[\widetilde{\mathbf{A}}(x - ct)e^{i(\omega_0 t - k_0 x)}]$, where $k_0 = \omega_0/c$. We denote this vector potential by $\widehat{\mathbf{A}}$; then $\hat{\mathbf{x}} \cdot \widehat{\mathbf{A}} = 0$. In the speed-of-light frame, this simplifies to $\widehat{\mathbf{A}}(\mathbf{x}') = \mathrm{Re}[\widetilde{\mathbf{A}}(\xi)e^{-ik_0\xi}]$.

The Hamiltonian in this case is

$$P_x = \frac{1}{2}\left(\frac{\left|\mathbf{P}_\perp - q\widehat{\mathbf{A}}\right|^2 + m^2c^2}{H'/c} - \frac{H'}{c}\right). \tag{50}$$

As this is depends only on the canonical momenta and ξ, not the canonical positions, the canonical momenta $\mathbf{P}_\perp$ and H' are constants of the motion. Thus the particle motion can be determined exactly as a function of ξ.

A.1.4. Perturbed motion

We now introduce the more general system: A particle in the field of a laser with fast oscillations in ξ modulated by a slowly-varying envelope, together with a slowly-varying background field. Thus we let $\mathbf{A} = \widehat{\mathbf{A}} + \overline{\mathbf{A}}$, where

$$\widehat{\mathbf{A}}(\mathbf{x}') = \mathrm{Re}\left[\widetilde{\mathbf{A}}(\mathbf{x}')e^{-ik_0\xi}\right]. \tag{51}$$

Here both $\widetilde{\mathbf{A}}$ and $\overline{\mathbf{A}}$ are slowly varying in all spacetime coordinates; we provide a more rigorous definition of "slowly-varying" below as we clearly define the problem.

Through our Hamiltonian formalism we can determine the equations of motion for the dynamic quantities τ, $\mathbf{x}_\perp$, $\mathbf{P}$, and H' as a function of ξ. Each of these quantities will have spectral components in narrow bands around integer multiples of the laser frequency k_0. Our goal, then, is to determine the motion of the particles averaged over the fast laser oscillations. We therefore define, for each dynamic variable ψ, its average $\bar{\psi}$ over ξ. For numerical purposes, we will need not just averages over ξ, but a set of dynamical equations which allow us to propagate the averaged phase-space coordinates of the particle forward in time.

To derive the averaged equations of motion, we start with the Hamiltonian for this system:

$$P_x = \frac{1}{2}\left(\frac{\left|\mathbf{P}_\perp - q\overline{\mathbf{A}}_\perp - q\widehat{\mathbf{A}}\right|^2 + m^2c^2}{H'/c - q\bar{\Phi}/c + q\overline{A}_x} - \frac{H'}{c} + q\frac{\bar{\Phi}}{c} + q\overline{A}_x\right). \tag{52}$$

We will proceed to derive the equations of motion from this Hamiltonian, and then average in ξ over a range on the order of a wavelength. The conditions we will need for the perturbation approximation, which define the term "slowly-varying," now become clear. We require that in any neighborhood of $(\xi, \tau, \mathbf{x}_\perp)$ space which a particle trajectory can cover while ξ varies on the scale of a wavelength, the variations in $\widetilde{\mathbf{A}}$, $\overline{\mathbf{A}}$, and $\bar{\Phi}$ are small enough that they can be treated perturbatively. We will specify these conditions precisely after we derive the equations of motion; in the meantime, we assume that they hold. Then since $\mathbf{P}_\perp$ and H' are constant in the unperturbed case, to leading order we can replace $\mathbf{P}_\perp$ and H' with $\overline{\mathbf{P}}_\perp$ and $\overline{H}'$, respectively, within the equations of motion.

A.1.5. Averaged kinetic quantities

To cast quantities that will appear in the equations of motion in more familiar terms, we define averaged kinetic quantities in terms of averaged canonical momenta. First, we define the averaged linear momentum by $\bar{\mathbf{p}} = \overline{\mathbf{P}} - \mathbf{q}\overline{\mathbf{A}}$. We can also define a quantity related to the average energy. We know that in terms of kinetic variables, the Hamiltonian in the lab frame is equal to the total particle energy, that is, $H = \gamma mc^2 + q\Phi$. We then have that $H' = \gamma mc^2 + q\Phi - cp_x - qcA_x$. With this in mind, we define the quantity $\bar{\gamma}$ such that

$$\overline{H}' = \bar{\gamma}mc^2 + q\bar{\Phi} - c\bar{p}_x - qc\overline{A}_x, \tag{53}$$

or

$$\frac{\overline{H}'}{c} - q\frac{\bar{\Phi}}{c} + q\overline{A}_x = \bar{\gamma}mc - \bar{p}_x. \tag{54}$$

We can obtain a more intuitive expression for γ by determining a relationship between $\bar{\mathbf{p}}$ and $\overline{H}'$. To do so we take the average of P_x. Denoting averages over ξ by $\langle\rangle$, and applying the perturbation approximation that allows us to replace canonical momenta with their averages, we have to leading order

$$\overline{P}_x = \frac{1}{2}\left\langle\frac{\left|\overline{\mathbf{P}}_\perp - q\overline{\mathbf{A}}_\perp - q\widehat{\mathbf{A}}\right|^2 + m^2c^2}{\overline{H}'/c - q\bar{\Phi}/c + q\overline{A}_x} - \frac{\overline{H}'}{c} + q\frac{\bar{\Phi}}{c} + q\overline{A}_x\right\rangle. \tag{55}$$

Then

$$\bar{p}_x = \overline{P}_x - q\overline{A}_x = \frac{1}{2}\left(\frac{\left\langle\left|\bar{\mathbf{p}}_\perp - q\widehat{\mathbf{A}}\right|^2\right\rangle + m^2c^2}{\bar{\gamma}mc - \bar{p}_x} - \frac{\overline{H}'}{c} + q\frac{\bar{\Phi}}{c} - q\overline{A}_x\right) = \frac{1}{2}\left[\frac{|\bar{\mathbf{p}}_\perp|^2 + q^2\left|\widetilde{\mathbf{A}}\right|^2/2 + m^2c^2}{\bar{\gamma}mc - \bar{p}_x} - (\bar{\gamma}mc - \bar{p}_x)\right], \tag{56}$$

so

$$2\bar{p}_x(\bar{\gamma}mc - \bar{p}_x) = |\bar{\mathbf{p}}_\perp|^2 + \frac{q^2\left|\widetilde{\mathbf{A}}\right|^2}{2} + m^2c^2 - (\bar{\gamma}mc - \bar{p}_x)^2, \tag{57}$$

$$2\bar{\gamma}mc\bar{p}_x - 2\bar{p}_x^2 = |\bar{\mathbf{p}}_\perp|^2 + \frac{q^2\left|\widetilde{\mathbf{A}}\right|^2}{2} + m^2c^2 - (\bar{\gamma}mc)^2 + 2\bar{\gamma}mc\bar{p}_x - \bar{p}_x^2, \tag{58}$$

and thus

$$(\bar{\gamma}mc)^2 = |\bar{\mathbf{p}}_\perp|^2 + \frac{q^2\left|\widetilde{\mathbf{A}}\right|^2}{2} + m^2c^2 + \bar{p}_x^2 = |\bar{\mathbf{p}}|^2 + \frac{q^2|\widetilde{\mathbf{A}}|^2}{2} + m^2c^2. \tag{59}$$

Therefore $\bar{\gamma}$ can be considered an averaged Lorentz factor for the particle, taking into account both the average momentum and the quiver energy.

A.1.6. Equations of motion

We can now derive the equations of motion averaged over the fast laser oscillations. We begin with τ. We have

$$\frac{d\tau}{d\xi} = \frac{\partial P_x}{\partial H'} = \frac{1}{2}\left[-\frac{\left|\mathbf{P}_\perp - q\overline{\mathbf{A}}_\perp - q\widehat{\mathbf{A}}\right|^2 + m^2c^2}{(H'/c - q\bar{\Phi}/c + q\overline{A}_x)^2}\cdot\frac{1}{c} - \frac{1}{c}\right]. \tag{60}$$

Applying the perturbation approximation and taking the average over ξ, we have

$$\frac{d\bar{\tau}}{d\xi} = -\frac{1}{2c}\left[\frac{|\bar{\mathbf{p}}_\perp|^2 + q^2\left|\widetilde{\mathbf{A}}\right|^2/2 + m^2c^2}{(\bar{\gamma}mc - \bar{p}_x)^2} + 1\right] = -\frac{1}{2c}\left[\frac{(\bar{\gamma}mc)^2 - \bar{p}_x^2}{(\bar{\gamma}mc - \bar{p}_x)^2} + 1\right] = -\frac{1}{2c}\left(\frac{\bar{\gamma}mc + \bar{p}_x}{\bar{\gamma}mc - \bar{p}_x} + 1\right) = -\frac{1}{2c}\cdot\frac{2\bar{\gamma}mc}{\bar{\gamma}mc - \bar{p}_x} = -\frac{\bar{\gamma}m}{\bar{\gamma}mc - \bar{p}_x}. \tag{61}$$

This equation of motion points a way around our problem of obtaining averaged time derivatives, when most of our expressions are written in terms of, and can only be easily averaged over, ξ. We know that $\bar{\tau}$ is monotonic in ξ, since Eq. (59) shows that $d\bar{\tau}/d\xi < 0$ everywhere. Thus we have, in $\bar{\tau}$, a function which is monotonically increasing with τ (since $d\xi/d\tau < 0$ everywhere), and which is slowly-varying with respect to ξ. The solution is therefore to express our equations of motion in terms of derivatives with respect to $\bar{\tau}$ rather than τ. We can easily obtain such equations by multiplying our expressions for derivatives with respect to ξ, obtained from the Hamilton equations, by

$$\frac{d\xi}{d\bar{\tau}} = -\frac{\bar{\gamma}mc - \bar{p}_x}{\bar{\gamma}m}. \tag{62}$$

We can immediately obtain an averaged equation of motion for the x coordinate. Defining $\bar{x} = \xi + c\bar{\tau}$, we have

$$\frac{d\bar{x}}{d\bar{\tau}} = \frac{d\xi}{d\bar{\tau}} + c = \frac{\bar{p}_x}{\bar{\gamma}m}. \tag{63}$$

The equations for the transverse position variables are also easily obtained. From Eq. (48), we have

$$\frac{d\mathbf{x}_\perp}{d\xi} = -\frac{\partial P_x}{\partial \mathbf{P}_\perp} = -\frac{1}{2}\left[\frac{2(\mathbf{P}_\perp - q\bar{\mathbf{A}}_\perp - q\widehat{\mathbf{A}})}{H'/c - q\bar{\Phi}/c + q\bar{A}_x}\right], \tag{64}$$

so that

$$\frac{d\bar{\mathbf{x}}_\perp}{d\xi} = -\frac{\bar{\mathbf{p}}_\perp}{\bar{\gamma}mc - \bar{p}_x}. \tag{65}$$

This gives

$$\frac{d\bar{\mathbf{x}}_\perp}{d\bar{\tau}} = \frac{\bar{\mathbf{p}}_\perp}{\bar{\gamma}m}, \tag{66}$$

so that we can define in general

$$\bar{\mathbf{v}} = \frac{d\bar{\mathbf{x}}}{d\bar{\tau}} = \frac{\bar{\mathbf{p}}}{\bar{\gamma}m}. \tag{67}$$

For the momentum variables, we have from Eq. (49) that

$$\frac{dP_i}{d\xi} = \frac{\partial P_x}{\partial x_i'} = \frac{1}{2}\left[\frac{2(\mathbf{P}_\perp - q\bar{\mathbf{A}}_\perp - q\widehat{\mathbf{A}})}{H'/c - q\bar{\Phi}/c + q\bar{A}_x}\cdot\left(-q\frac{\partial\widehat{\mathbf{A}}}{\partial x_i'} - q\frac{\partial\bar{\mathbf{A}}_\perp}{\partial x_i'}\right) - \frac{\left|\mathbf{P}_\perp - q\bar{\mathbf{A}}_\perp - q\widehat{\mathbf{A}}\right|^2 + m^2c^2}{(H'/c - q\bar{\Phi}/c + q\bar{A}_x)^2}\left(-\frac{q}{c}\frac{\partial\bar{\Phi}}{\partial x_i'} + q\frac{\partial\bar{A}_x}{\partial x_i'}\right) + \frac{q}{c}\frac{\partial\bar{\Phi}}{\partial x_i'} + q\frac{\partial\bar{A}_x}{\partial x_i'}\right], \tag{68}$$

so

$$\frac{d\bar{P}_i}{d\xi} = \frac{1}{2}\left[\frac{2(\bar{\mathbf{P}}_\perp - q\bar{\mathbf{A}}_\perp)\cdot\left(-q\partial\bar{\mathbf{A}}_\perp/\partial x_i'\right) + q^2\partial\left\langle|\widehat{\mathbf{A}}|^2\right\rangle/\partial x_i'}{\bar{H}'/c - q\bar{\Phi}/c + q\bar{A}_x} - \frac{\left|\bar{\mathbf{P}}_\perp - q\bar{\mathbf{A}}_\perp\right|^2 + q^2\left|\widetilde{\mathbf{A}}\right|^2 + m^2c^2}{(\bar{H}'/c - q\bar{\Phi}/c + q\bar{A}_x)^2}\left(-\frac{q}{c}\frac{\partial\bar{\Phi}}{\partial x_i'} + q\frac{\partial\bar{A}_x}{\partial x_i'}\right) + \frac{q}{c}\frac{\partial\bar{\Phi}}{\partial x_i'} + q\frac{\partial\bar{A}_x}{\partial x_i'}\right]. \tag{69}$$

This gives, in terms of kinetic variables,

$$\begin{aligned}
\frac{d\bar{P}_i}{d\xi} &= \frac{1}{2}\left[\frac{1}{\bar{\gamma}mc - \bar{p}_x}\left(-2q\bar{\mathbf{p}}_\perp\cdot\frac{\partial\bar{\mathbf{A}}_\perp}{\partial x_i'} + \frac{q^2}{2}\frac{\partial}{\partial x_i'}\left|\widetilde{\mathbf{A}}\right|^2\right) - \frac{(\bar{\gamma}mc)^2 - \bar{p}_x^2}{(\bar{\gamma}mc - \bar{p}_x)^2}\left(-\frac{q}{c}\frac{\partial\bar{\Phi}}{\partial x_i'} + q\frac{\partial\bar{A}_x}{\partial x_i'}\right) + \frac{q}{c}\frac{\partial\bar{\Phi}}{\partial x_i'} + q\frac{\partial\bar{A}_x}{\partial x_i'}\right] \\
&= \frac{1}{2}\left[\frac{1}{\bar{\gamma}mc - \bar{p}_x}\left(-2q\bar{\mathbf{p}}_\perp\cdot\frac{\partial\bar{\mathbf{A}}_\perp}{\partial x_i'} + \frac{q^2}{2}\frac{\partial}{\partial x_i'}\left|\widetilde{\mathbf{A}}\right|^2\right) + \left(\frac{\bar{\gamma}mc + \bar{p}_x}{\bar{\gamma}mc - \bar{p}_x} + 1\right)\frac{q}{c}\frac{\partial\bar{\Phi}}{\partial x_i'} - \left(\frac{\bar{\gamma}mc + \bar{p}_x}{\bar{\gamma}mc - \bar{p}_x} - 1\right)q\frac{\partial\bar{A}_x}{\partial x_i'}\right] \\
&= \frac{1}{\bar{\gamma}mc - \bar{p}_x}\left(-q\bar{\mathbf{p}}_\perp\cdot\frac{\partial\bar{\mathbf{A}}_\perp}{\partial x_i'} + \frac{q^2}{4}\frac{\partial}{\partial x_i'}\left|\widetilde{\mathbf{A}}\right|^2 + \bar{\gamma}mq\frac{\partial\bar{\Phi}}{\partial x_i'} - q\bar{p}_x\frac{\partial\bar{A}_x}{\partial x_i'}\right) = \frac{1}{\bar{\gamma}mc - \bar{p}_x}\left(-q\bar{\mathbf{p}}\cdot\frac{\partial\bar{\mathbf{A}}}{\partial x_i'} + \frac{q^2}{4}\frac{\partial}{\partial x_i'}\left|\widetilde{\mathbf{A}}\right|^2 + \bar{\gamma}mq\frac{\partial\bar{\Phi}}{\partial x_i'}\right).
\end{aligned} \tag{70}$$

We then have

$$\frac{d\overline{P}_i}{d\tau}=\frac{d\xi}{d\tau}\frac{d\overline{P}_i}{d\xi}=-\frac{1}{\bar{\gamma}m}\left(-q\bar{\mathbf{p}}\cdot\frac{\partial\overline{\mathbf{A}}}{\partial x_i'}+\frac{q^2}{4}\frac{\partial}{\partial x_i'}\left|\widetilde{\mathbf{A}}\right|^2+\bar{\gamma}mq\frac{\partial\bar{\Phi}}{\partial x_i'}\right)=q\bar{\mathbf{v}}\cdot\frac{\partial\overline{\mathbf{A}}}{\partial x_i'}-\frac{q^2}{4\bar{\gamma}m}\frac{\partial}{\partial x_i'}\left|\widetilde{\mathbf{A}}\right|^2-q\frac{\partial\bar{\Phi}}{\partial x_i'}. \tag{71}$$

For a slowly-varying field ψ we can write

$$\frac{d\psi}{d\tau}=\frac{\partial\psi}{\partial t}+\bar{\mathbf{v}}\cdot\nabla\psi, \tag{72}$$

and using the fact from Eq. (34) that $\partial/\partial x_i'=\partial/\partial x_i$, we have

$$\frac{d\bar{p}_i}{d\tau}+q\frac{\partial\overline{A}_i}{\partial t}+\bar{\mathbf{v}}\cdot\nabla\overline{A}_i=q\bar{\mathbf{v}}\cdot\frac{\partial\overline{\mathbf{A}}}{\partial x_i}-\frac{q^2}{4\bar{\gamma}m}\frac{\partial}{\partial x_i}\left|\widetilde{\mathbf{A}}\right|^2-q\frac{\partial\bar{\Phi}}{\partial x_i}, \tag{73}$$

so that

$$\frac{d\bar{p}_i}{d\tau}=q\left(-\frac{\partial\overline{A}_i}{\partial t}-\frac{\partial\bar{\Phi}}{\partial x_i}+\bar{\mathbf{v}}\cdot\frac{\partial\overline{\mathbf{A}}}{\partial x_i}-\bar{\mathbf{v}}\cdot\nabla\overline{A}_i\right)-\frac{q^2}{4\bar{\gamma}m}\frac{\partial}{\partial x_i}\left|\widetilde{\mathbf{A}}\right|^2. \tag{74}$$

Now, assuming repeated indices are summed over,

$$\bar{\mathbf{v}}\cdot\frac{\partial\overline{\mathbf{A}}}{\partial x_i}-\bar{\mathbf{v}}\cdot\nabla\overline{A}_i=\bar{v}_j\partial_i\overline{A}_j-\bar{v}_j\partial_j\overline{A}_i=\bar{v}_j(\delta_{il}\delta_{jm}-\delta_{im}\delta_{jl})\partial_l\overline{A}_m=\bar{v}_j\epsilon_{ijk}\epsilon_{lmk}\partial_l\overline{A}_m=\epsilon_{ijk}\bar{v}_j(\nabla\times\overline{\mathbf{A}})_k=\left[\bar{\mathbf{v}}\times(\nabla\times\overline{\mathbf{A}})\right]_i. \tag{75}$$

Then

$$\frac{d\bar{p}_i}{d\tau}=q(\overline{\mathbf{E}}+\bar{\mathbf{v}}\times\overline{\mathbf{B}})_i-\frac{q^2}{4\bar{\gamma}m}\frac{\partial}{\partial x_i}\left|\widetilde{\mathbf{A}}\right|^2, \tag{76}$$

or

$$\frac{d\bar{\mathbf{p}}}{d\tau}=q(\overline{\mathbf{E}}+\bar{\mathbf{v}}\times\overline{\mathbf{B}})-\frac{q^2}{4\bar{\gamma}m}\nabla\left|\widetilde{\mathbf{A}}\right|^2. \tag{77}$$

This is the ponderomotive force with a background field.

We can check these equations by examining the motion of H'. From Eq. (49), we have

$$\frac{dH'}{d\xi}=-\frac{\partial P_x}{\partial\tau}=-\frac{1}{2}\left[\frac{2(\mathbf{P}_\perp-q\overline{\mathbf{A}}_\perp-q\widehat{\mathbf{A}})}{H'/c-q\bar{\Phi}/c+q\overline{A}_x}\cdot\left(-q\frac{\partial\widehat{\mathbf{A}}}{\partial\tau}-q\frac{\partial\overline{\mathbf{A}}_\perp}{\partial\tau}\right)-\frac{\left|\mathbf{P}_\perp-q\overline{\mathbf{A}}_\perp-q\widehat{\mathbf{A}}\right|^2+m^2c^2}{(H'/c-q\bar{\Phi}/c+q\overline{A}_x)^2}\left(-\frac{q}{c}\frac{\partial\bar{\Phi}}{\partial\tau}+q\frac{\partial\overline{A}_x}{\partial\tau}\right)+\frac{q}{c}\frac{\partial\bar{\Phi}}{\partial\tau}+q\frac{\partial\overline{A}_x}{\partial\tau}\right]. \tag{78}$$

This has the same form as Eq. (68), with x_i' replaced with τ and with the opposite sign. Through the same manipulations, we then arrive at

$$\frac{d\overline{H}'}{d\xi}=\frac{1}{\bar{\gamma}mc-\bar{p}_x}\left(q\bar{\mathbf{p}}\cdot\frac{\partial\overline{\mathbf{A}}}{\partial\tau}-\frac{q^2}{4}\frac{\partial}{\partial\tau}\left|\widetilde{\mathbf{A}}\right|^2-\bar{\gamma}mq\frac{\partial\bar{\Phi}}{\partial\tau}\right), \tag{79}$$

so

$$\frac{d\overline{H}'}{d\tau}=-q\bar{\mathbf{v}}\cdot\frac{\partial\overline{\mathbf{A}}}{\partial\tau}+\frac{q^2}{4\bar{\gamma}m}\frac{\partial}{\partial\tau}\left|\widetilde{\mathbf{A}}\right|^2+q\frac{\partial\bar{\Phi}}{\partial\tau}. \tag{80}$$

Applying Eq. (34), we have

$$\begin{aligned}\frac{d\overline{H}'}{d\tau}&=-q\bar{\mathbf{v}}\cdot\frac{\partial\overline{\mathbf{A}}}{\partial t}+\frac{q^2}{4\bar{\gamma}m}\frac{\partial}{\partial t}\left|\widetilde{\mathbf{A}}\right|^2+q\frac{\partial\bar{\Phi}}{\partial t}-c\left(q\bar{\mathbf{v}}\cdot\frac{\partial\overline{\mathbf{A}}}{\partial x}-\frac{q^2}{4\bar{\gamma}m}\frac{\partial}{\partial x}\left|\widetilde{\mathbf{A}}\right|^2-q\frac{\partial\bar{\Phi}}{\partial x}\right)\\&=-q\bar{\mathbf{v}}\cdot\frac{\partial\overline{\mathbf{A}}}{\partial t}+\frac{q^2}{4\bar{\gamma}m}\frac{\partial}{\partial t}\left|\widetilde{\mathbf{A}}\right|^2+q\frac{\partial\bar{\Phi}}{\partial t}-c\frac{d\overline{P}_x}{d\tau}\end{aligned} \tag{81}$$

by Eq. (71). Then using the fact that $\overline{H}'=\bar{\gamma}mc^2+q\bar{\Phi}-c\overline{P}_x$ and Eq. (72), we have

$$\frac{d}{d\tau}(\bar{\gamma}mc^2)=\frac{d\overline{H}'}{d\tau}+c\frac{d\overline{P}_x}{d\tau}-q\frac{d\bar{\Phi}}{d\tau}=-q\bar{\mathbf{v}}\cdot\frac{\partial\overline{\mathbf{A}}}{\partial t}+\frac{q^2}{4\bar{\gamma}m}\frac{\partial}{\partial t}\left|\widetilde{\mathbf{A}}\right|^2-q\bar{\mathbf{v}}\cdot\nabla\bar{\Phi}=q\bar{\mathbf{v}}\cdot\overline{\mathbf{E}}+\frac{q^2}{4\bar{\gamma}m}\frac{\partial}{\partial t}\left|\widetilde{\mathbf{A}}\right|^2. \tag{82}$$

We can check this from the equations of motion for $\bar{\mathbf{p}}$. We have from Eq. (59) that

$$\bar{\gamma}mc^2 = c\sqrt{|\bar{\mathbf{p}}|^2 + \frac{q^2\left|\widetilde{\mathbf{A}}\right|^2}{2} + m^2c^2}, \tag{83}$$

so

$$\begin{aligned}\frac{d}{d\bar{\tau}}(\bar{\gamma}mc^2) &= \frac{c}{2\bar{\gamma}mc}\left(2\bar{\mathbf{p}}\cdot\frac{d\bar{\mathbf{p}}}{d\bar{\tau}} + \frac{q^2}{2}\frac{d}{d\bar{\tau}}\left|\widetilde{\mathbf{A}}\right|^2\right) = \bar{\mathbf{v}}\cdot\left[q(\overline{\mathbf{E}} + \bar{\mathbf{v}}\times\overline{\mathbf{B}}) - \frac{q^2}{4\bar{\gamma}m}\nabla\left|\widetilde{\mathbf{A}}\right|^2\right] + \frac{q^2}{4\bar{\gamma}m}\left(\frac{\partial}{\partial t}\left|\widetilde{\mathbf{A}}\right|^2 + \bar{\mathbf{v}}\cdot\nabla\left|\widetilde{\mathbf{A}}\right|^2\right)\\ &= q\bar{\mathbf{v}}\cdot\overline{\mathbf{E}} + \frac{q^2}{4\bar{\gamma}m}\frac{\partial}{\partial t}\left|\widetilde{\mathbf{A}}\right|^2.\end{aligned} \tag{84}$$

Thus the average energy evolution equation from the Hamiltonian formalism is consistent with those for the momentum.

A.1.7. The perturbative approximation

Now that we have used our perturbation approximations to derive the equations of motion, we can specify a set of conditions which are sufficient for making those approximations valid. As mentioned above, we must have that the variations of all the potentials are small enough to be treated perturbatively in a neighborhood of spacetime traversed by a particle in a time on the order of a single oscillation. These conditions are simplified by requiring that such a neighborhood is on the order of a wavelength in all directions, which itself yields our first condition. From Eq. (64), we have that to leading order,

$$\frac{d\mathbf{x}_\perp}{d\xi} = -\frac{\bar{\mathbf{p}}_\perp - q\widehat{\mathbf{A}}}{\bar{\gamma}mc - \bar{p}_x}. \tag{85}$$

For the transverse deviation of the particle over a single oscillation to be on the order of the wavelength λ, this quantity must be of order unity. We know from Eq. (59) that $|\bar{\mathbf{p}}_\perp - q\widehat{\mathbf{A}}| \leqslant \mathcal{O}(1)\bar{\gamma}mc$, so we require that

$$\left|\frac{\bar{\gamma}mc}{\bar{\gamma}mc - \bar{p}_x}\right| = \frac{1}{|1 - \bar{v}_x/c|} = \mathcal{O}(1). \tag{86}$$

This requirement makes sense because the amplitude of the transverse oscillations of a particle are on the order of a wavelength in the particle's rest frame. If a particle has highly relativistic average motion in the $+x$ direction, the optical wavelength is dilated by $\gamma(1+\beta)$, so the transverse oscillations are increased by that factor. Note that this requirement does not imply that $|v_x| \ll c$; it merely implies that particles cannot be moving highly relativistically in the direction of the laser. In addition, this restriction only applies to the direct interaction between particles and the laser field, not to particles experiencing only the wake. Therefore beam particles that are not in the laser field are modeled correctly. However, the envelope model does not correctly capture the transverse dynamics of beam particles which experience strong laser fields, a phenomenon explored in [48].

Once we have required that a particle is confined to a spacetime region on the order of an optical wavelength in a single oscillation cycle, our remaining requirement for the perturbation is the slowly-varying approximation on the potentials. If we let A be $\bar{\Phi}$ or any component of $\overline{\mathbf{A}}$ or $\widetilde{\mathbf{A}}$, and letting r denote a spacetime vector, we require that on average

$$\lambda\left|\frac{\partial^2 A}{\partial r^2}\right| \ll \left|\frac{\partial A}{\partial r}\right|. \tag{87}$$

In other words, as long as the ponderomotive force and the background electromagnetic fields do not change significantly on the scale of an optical wavelength, the perturbation approximation should be valid.

A.2. Envelope evolution

We now derive the evolution of the transverse vector potential envelope itself. First, we justify a further approximation we have made in the Hamiltonian, Eq. (52), namely, that we ignore the oscillatory part $\tilde{\Phi}$ of the scalar potential. To do so, we compute $\tilde{\Phi}$ to lowest order, and specify the assumption necessary to make the approximation valid. In the Coulomb gauge, we have the Poisson equation $\nabla^2\Phi = \rho/\epsilon_0$, where ρ is the charge density. Since we assume that the envelopes of the oscillatory components of the fields vary slowly relative to the optical wavelength, we have to lowest order

$$\frac{\rho}{\epsilon_0} = k_0^2\tilde{\Phi}; \tag{88}$$

then

$$\frac{\tilde{\Phi}}{c} = \frac{\rho}{k_0^2\epsilon_0 c} = \frac{nq}{k_0^2\epsilon_0 c}, \tag{89}$$

where n is the plasma number density. Now the plasma wavenumber k_p is given by

$$k_p^2 = \frac{nq^2}{m\epsilon_0 c^2}. \tag{90}$$

Thus we can write

$$\frac{\tilde{\Phi}}{c} = \frac{mc}{q}\frac{k_p^2}{k_0^2}. \tag{91}$$

We therefore assume that $|\widetilde{\mathbf{A}}_\perp| \sim mc/q$, that $k_p \ll k_0$, and that we are computing the envelope evolution equation to lowest order in k_p/k_0. Then $\tilde{\Phi}/c$ is a second-order perturbation relative to $\widetilde{\mathbf{A}}$, and we ignore it.

With this approximation, we can now derive the equation of motion for the laser pulse envelope. We use the notation $\widehat{\mathbf{E}}$, $\widehat{\mathbf{B}}$ to denote the oscillating components of the electromagnetic fields just as we do for $\widehat{\mathbf{A}}$. The oscillating fields are then derived from the vector potential by

$$\widehat{\mathbf{E}} = -\frac{\partial \widehat{\mathbf{A}}}{\partial t}, \quad \widehat{\mathbf{B}} = \nabla \times \widehat{\mathbf{A}}. \tag{92}$$

Starting in the lab frame, we then have

$$\frac{1}{c^2}\frac{\partial^2 \widehat{\mathbf{A}}}{\partial t^2} = -\frac{1}{c^2}\frac{\partial \widehat{\mathbf{E}}}{\partial t} = -\nabla \times \widehat{\mathbf{B}} + \mu_0 \widehat{\mathbf{J}} = -\nabla \times (\nabla \times \widehat{\mathbf{A}}) + \mu_0 \widehat{\mathbf{J}} = -\nabla(\nabla \cdot \widehat{\mathbf{A}}) + \nabla^2 \widehat{\mathbf{A}} + \mu_0 \widehat{\mathbf{J}}. \tag{93}$$

Applying the Coulomb gauge condition, we then have

$$\frac{1}{c^2}\frac{\partial^2 \widehat{\mathbf{A}}}{\partial t^2} - \nabla^2 \widehat{\mathbf{A}} = \mu_0 \widehat{\mathbf{J}}. \tag{94}$$

We now transition to the speed-of-light frame, using Eq. (35). This gives

$$\mu_0 \widehat{\mathbf{J}} = \left[\left(\frac{1}{c}\frac{\partial}{\partial \tau} - \frac{\partial}{\partial \xi}\right)^2 - \frac{\partial^2}{\partial \xi^2} - \nabla_\perp^2\right]\widehat{\mathbf{A}} = \left(\frac{1}{c^2}\frac{\partial^2}{\partial \tau^2} - \frac{2}{c}\frac{\partial}{\partial \tau}\frac{\partial}{\partial \xi} + \frac{\partial^2}{\partial \xi^2} - \frac{\partial^2}{\partial \xi^2} - \nabla_\perp^2\right)\widehat{\mathbf{A}} = \left(\frac{1}{c^2}\frac{\partial^2}{\partial \tau^2} - \frac{2}{c}\frac{\partial}{\partial \tau}\frac{\partial}{\partial \xi} - \nabla_\perp^2\right)\widehat{\mathbf{A}}. \tag{95}$$

Next, we apply the relation $\widehat{\mathbf{A}} = \mathrm{Re}(\widetilde{\mathbf{A}} e^{-ik_0\xi})$, and a similar relation for $\widehat{\mathbf{J}}$, to arrive at

$$\frac{1}{c^2}\frac{\partial^2 \widetilde{\mathbf{A}}}{\partial \tau^2} - \frac{2}{c}\frac{\partial}{\partial \tau}\left(\frac{\partial \widetilde{\mathbf{A}}}{\partial \xi} - ik_0 \widetilde{\mathbf{A}}\right) - \nabla_\perp^2 \widetilde{\mathbf{A}} = \mu_0 \widetilde{\mathbf{J}}. \tag{96}$$

We can use the slowly-varying envelope approximation, Eq. (87), that we required as part of the perturbative treatment, to drop the first term in this equation, to give

$$\frac{2}{c}\frac{\partial}{\partial \tau}\left(\frac{\partial \widetilde{\mathbf{A}}}{\partial \xi} - ik_0 \widetilde{\mathbf{A}}\right) + \nabla_\perp^2 \widetilde{\mathbf{A}} = -\mu_0 \widetilde{\mathbf{J}}. \tag{97}$$

Finally, we establish a linear relationship between $\widetilde{\mathbf{J}}$ and $\widetilde{\mathbf{A}}$ to self-consistently describe the evolution of $\widetilde{\mathbf{A}}$. As the current density due to a single particle is proportional to its velocity, we must compute the oscillatory part of the particle velocity. To do so, we begin from the relation, derived from the light-frame Hamiltonian, used to derive the average velocity, namely Eq. (64). Taking the oscillatory part of this relation gives, to lowest order in our perturbation approximation,

$$\frac{d\hat{\mathbf{x}}_\perp}{d\xi} = \frac{q\widehat{\mathbf{A}}}{\bar{\gamma}mc - \bar{p}_x}, \tag{98}$$

which, when combined with Eq. (62), yields

$$\frac{d\hat{\mathbf{x}}_\perp}{d\bar{\tau}} = -\frac{q\widehat{\mathbf{A}}}{\bar{\gamma}m}. \tag{99}$$

A particle propagating with velocity $\mathbf{v}$ induces current density $\rho\mathbf{v}$, where ρ is the charge density associated with the particle. The oscillatory current density from the ith particle is therefore related to the local oscillatory vector potential by

$$\widetilde{\mathbf{J}}_i = -\frac{q\rho_i}{\bar{\gamma}_i m}\widetilde{\mathbf{A}}, \tag{100}$$

and for an ensemble of plasma particles we then have

$$\widetilde{\mathbf{J}} = \left(-\sum_i \frac{q\rho_i}{\bar{\gamma}_i m}\right)\widetilde{\mathbf{A}}. \tag{101}$$

With this relationship we can define a susceptibility for the plasma analogous to the susceptibility of a dielectric material. For a dielectric, we have a susceptibility χ defined by $\mathbf{P} = \epsilon_0\chi\mathbf{E}$. For a single-frequency oscillation, we then have

$$\widetilde{\mathbf{J}} = i\omega_0\widetilde{\mathbf{P}} = i\omega_0\epsilon_0\chi\widetilde{\mathbf{E}} = i\omega_0\epsilon_0\chi(-i\omega_0\widetilde{\mathbf{A}}) = \omega_0^2\epsilon_0\chi\widetilde{\mathbf{A}} = k_0^2c^2\epsilon_0\chi\widetilde{\mathbf{A}} = \frac{k_0^2}{\mu_0}\widetilde{\mathbf{A}}. \tag{102}$$

We therefore define the *plasma susceptibility* by

$$\chi = -\frac{\mu_0}{k_0^2}\sum_i \frac{q\rho_i}{\bar{\gamma}_i m}; \tag{103}$$

then $\widetilde{\mathbf{J}} = (k_0^2/\mu_0)\chi\widetilde{\mathbf{A}}$, so

$$\left[\frac{2}{c}\frac{\partial}{\partial\tau}\left(\frac{\partial}{\partial\xi} - ik_0\right) + \nabla_\perp^2\right]\widetilde{\mathbf{A}} = -k_0^2\chi\widetilde{\mathbf{A}}. \tag{104}$$

We normalize this equation so the operators on both sides are dimensionless, and the dominant term, currently the one with $-ik_0$ on the LHS, becomes unity. We thus multiply both sides by i/k_0^2 to obtain

$$\left[\frac{2}{\omega_0}\frac{\partial}{\partial\tau}\left(1 + \frac{i}{k_0}\frac{\partial}{\partial\xi}\right) + \frac{i}{k_0^2}\nabla_\perp^2\right]\widetilde{\mathbf{A}} = -i\chi\widetilde{\mathbf{A}}. \tag{105}$$

This describes the time-evolution of the laser envelope field.

References

[1] T. Tajima, J.M. Dawson, Laser electron accelerator, Phys. Rev. Lett. 43 (4) (1979) 267–270, doi:10.1103/PhysRevLett.43.267.
[2] E. Esarey, C.B. Schroeder, W.P. Leemans, Physics of laser-driven plasma-based electron accelerators, Rev. Mod. Phys. 81 (3) (2009) 1229–1285. doi:10.1103/RevModPhys.81.1229. URL: <http://link.aps.org/abstract/RMP/v81/p1229>.
[3] P. Sprangle, E. Esarey, A. Ting, Nonlinear theory of intense laser–plasma interactions, Phys. Rev. Lett. 64 (17) (1990) 2011–2014, doi:10.1103/PhysRevLett.64.2011.
[4] C.G.R. Geddes, C. Toth, J. van Tilborg, E. Esarey, C.B. Schroeder, D.L. Bruhwiler, C. Nieter, J.R. Cary, W. Leemans, High-quality electron beams from a laser wakefield accelerator using plasma-channel guiding, Nature 431 (2004) 538.
[5] S.P.D. Mangles, C.D. Murphy, Z. Najmudin, A.G.R. Thomas, J.L. Collier, A.E. Dangor, E.J. Divall, P.S. Foster, J.G. Gallacher, C.J. Hooker, D.A. Jaroszynski, A.J. Langley, W.B. Mori, P.A. Norreys, F.S. Tsung, R. Viskup, B.R. Walton, K. Krushelnick, Monoenergetic beams of relativistic electrons from intense laser–plasma interactions, Nature 431 (2004) 535.
[6] J. Faure, Y. Glinec, A. Pukhov, S. Kiselev, S. Gordienko, E. Lefebvre, J.-P. Rousseau, F. Burgy, V. Malka, A laser–plasma accelerator producing monoenergetic electron beams, Nature 431 (2004) 541.
[7] C.B. Schroeder, E. Esarey, C.G.R. Geddes, C. Toth, W.P. Leemans, Design considerations for a laser–plasma linear collider, in: C.B. Schroeder, W.P. Leemans, E. Esarey (Eds.), Thirteenth Advanced Accelerator Concepts, Santa Cruz, CA, 2008, American Institute of Physics, Melville, NY, 2009, pp. 208–214.
[8] F.V. Hartemann, D.J. Gibson, W.J. Brown, A. Rousse, K.T. Phuoc, V. Mallka, J. Faure, A. Pukhov, Compton scattering X-ray sources driven by laser wakefield acceleration, Phys. Rev. ST Accel. Beams 10 (1) (2007) 011301, doi:10.1103/PhysRevSTAB.10.011301.
[9] F. Grüner, S. Becker, U. Schramm, T. Eichner, M. Fuchs, R. Weingartner, D. Habs, J. Meyer-ter-Vehn, M. Geissler, M. Ferrario, L. Serafini, B. van der Geer, H. Backe, W. Lauth, S. Reiche, Design considerations for table-top, laser-based VUV and X-ray free electron lasers, Appl. Phys. B 86 (3) (2007) 431–435.
[10] C.B. Schroeder, W.M. Fawley, E. Esarey, W.P. Leemans, Design of an XUV FEL driven by the laser–plasma accelerator at the LBNL LOASIS facility, in: Proceedings of FEL 2006, JACoW, 2006, pp. 455–458. URL: <www.JACoW.org>.
[11] .A. Jaroszynski, R. Bingham, E. Brunetti, B. Ersfeld, J. Gallacher, B. van der Geer, R. Issac, S.P. Jamison, D. Jones, M. de Loos, A. Lyachev, V. Pavlov, A. Reitsma, Y. Saveliev, G. Vieux, S.M. Wiggins, Radiation sources based on laser–plasma interactions, Philos. Trans. Roy. Soc. London, Ser. A 364 (2006) 689–710.
[12] W.P. Leemans, B. Nagler, A.J. Gonsalves, C. Toth, K. Nakamura, C.G.R. Geddes, E. Esarey, C.B. Schroeder, S.M. Hooker, GeV electron beams from a centimetre-scale accelerator, Nat. Phys. 2 (10) (2006) 696–699. URL: <http://dx.doi.org/10.1038/nphys418>.
[13] C.G.R. Geddes, K. Nakamura, G.R. Plateau, C. Toth, E. Cormier-Michel, E. Esarey, C.B. Schroeder, J.R. Cary, W.P. Leemans, Plasma-density-gradient injection of low absolute-momentum-spread electron bunches, Phys. Rev. Lett. 100 (21) (2008) 215004. doi:10.1103/PhysRevLett.100.215004. URL: <http://link.aps.org/abstract/PRL/v100/e215004>.
[14] J. Faure, C. Rechatin, A. Norlin, A. Lifschitz, Y. Glinec, V. Malka, Controlled injection and acceleration of electrons in plasma wakefields by colliding laser pulses, Nature 444 (7120) (2006) 737–739. URL: <http://dx.doi.org/10.1038/nature05393>.
[15] C.K. Birdsall, A.B. Langdon, Plasma Physics via Computer Simulation, McGraw-Hill, New York, NY, 1985.
[16] R.W. Hockney, J.W. Eastwood, Computer Simulation Using Particles, McGraw-Hill, New York, NY, 1981.
[17] K.S. Yee, Numerical solution of initial boundary value problems involving Maxwell's equations in isotropic media, IEEE Trans. Anten. Propag. 14 (3) (1966) 302–307.
[18] A. Taflove, S.C. Hagness, Computational Electrodynamics: The Finite-Difference Time-Domain Method, second ed., Artech House, Boston, 2000.
[19] J. Villasenor, O. Buneman, Rigorous charge conservation for local electromagnetic field solvers, Comput. Phys. Commun. 69 (2–3) (1992) 306–316. URL: <http://www.sciencedirect.com/science/article/B6TJ5-46G8DM8-FH/2/69001c21b1cc777b5ddd573b1ac2b9d6>.
[20] T.Z. Esirkepov, Exact charge conservation scheme for particle-in-cell simulation with an arbitrary form-factor, Comput. Phys. Commun. 135 (2) (2001) 144–153. URL: <http://www.sciencedirect.com/science/article/B6TJ5-42MN624-2/2/901300107b9ab686926d99acbedeed56>.
[21] C.G.R. Geddes, D.L. Bruhwiler, J.R. Cary, W.B. Mori, J.-L. Vay, S.F. Martins, T. Katsouleas, E. Cormier-Michel, W.M. Fawley, C. Huang, X. Wang, B. Cowan, V.K. Decyk, E. Esarey, R.A. Fonseca, W. Lu, P. Messmer, P. Mullowney, K. Nakamura, K. Paul, G.R. Plateau, C.B. Schroeder, L.O. Silva, C. Toth, F.S. Tsung, M. Tzoufras, T. Antonsen, J. Vieira, W.P. Leemans, Computational studies and optimization of wakefield accelerators, J. Phys.: Conf. Ser. 125 (2008) 012002. URL: <http://stacks.iop.org/1742-6596/125/012002>.
[22] J. Krall, A. Ting, E. Esarey, P. Sprangle, Enhanced acceleration in a self-modulated-laser wake-field accelerator, Phys. Rev. E 48 (3) (1993) 2157–2161, doi:10.1103/PhysRevE.48.2157.
[23] P. Mora, T.M. Antonsen, Jr., Kinetic modeling of intense, short laser pulses propagating in tenuous plasmas, Phys. Plasmas 4 (1) (1997) 217–229. doi:10.1063/1.872134. URL: <http://link.aip.org/link/?PHP/4/217/1>.

[24] C. Huang, V.K. Decyk, C. Ren, M. Zhou, W. Lu, W.B. Mori, J.H. Cooley, T.M. Antonsen, Jr., T. Katsouleas, QUICKPIC: a highly efficient particle-in-cell code for modeling wakefield acceleration in plasmas, J. Comput. Phys. 217 (2) (2006) 658–679. URL: <http://www.sciencedirect.com/science/article/B6WHY-4JGJGXS-1/2/49765f434355b2b0771658fe96ce8552>.
[25] J.-L. Vay, Noninvariance of space- and time-scale ranges under a Lorentz transformation and the implications for the study of relativistic interactions, Phys. Rev. Lett. 98 (13) (2007) 130405. doi:10.1103/PhysRevLett.98.130405. URL: <http://link.aps.org/abstract/PRL/v98/e130405>.
[26] D.L. Bruhwiler, J.R. Cary, B. Cowan, K. Paul, C.G.R. Geddes, P.J. Mullowney, P. Messmer, E. Esarey, E. Cormier-Michel, W.P. Leemans, J.-L. Vay, New developments in the simulation of advanced accelerator concepts, in: C.B. Schroeder, W.P. Leemans, E. Esarey (Eds.), Thirteenth Advanced Accelerator Concepts, Santa Cruz, CA, 2008, American Institute of Physics, Melville, NY, 2009, pp. 29–37.
[27] S.F. Martins, R.A. Fonseca, W. Lu, W.B. Mori, L. Silva, Exploring laser-wakefield-accelerator regimes for near-term lasers using particle-in-cell simulation in Lorentz-boosted frames, Nat. Phys. 6 (2010) 311.
[28] S.F. Martins, R.A. Fonseca, L.O. Silva, W. Lu, W.B. Morri, Numerical simulations of laser wakefield accelerators in optimal Lorentz frames, Comput. Phys. Commun. 181 (2010) 869.
[29] S.F. Martins, R.A. Fonseca, J. Vieira, L.O. Silva, W. Lu, W.B. Mori, Modeling laser wakefield accelerator experiments with ultrafast particle-in-cell simulations in boosted frames, Phys. Plasmas 17 (2010) 056705.
[30] D. Gordon, W. Mori, T. Antonsen Jr., A ponderomotive guiding center particle-in-cell code for efficient modeling of laser–plasma interactions, IEEE Trans. Plasma Sci. 28 (4) (2000) 1135–1143, doi:10.1109/27.893300.
[31] C. Nieter, J.R. Cary, VORPAL: a versatile plasma simulation code, J. Comput. Phys. 196 (2004) 538.
[32] P. Messmer, D.L. Bruhwiler, Simulating laser pulse propagation and low-frequency wave emission in capillary plasma channel systems with a ponderomotive guiding center model, Phys. Rev. ST Accel. Beams 9 (3) (2006) 031302, doi:10.1103/PhysRevSTAB.9.031302.
[33] D. Gordon, Improved ponderomotive guiding center algorithm, IEEE Trans. Plasma Sci. 35 (5) (2007) 1486–1488, doi:10.1109/TPS.2007.905949.
[34] M.A. Heroux, J.M. Willenbring, Trilinos users guide, Tech. Rep. SAND2003-2952, Sandia National Laboratories, 2003.
[35] E. Esarey, P. Sprangle, J. Krall, A. Ting, Self-focusing and guiding of short laser pulses in ionizing gases and plasmas, IEEE J. Quantum Electron. 33 (11) (1997) 1879–1914, doi:10.1109/3.641305.
[36] A.E. Siegman, Lasers, University Science Books, Mill Valley, CA, 1986.
[37] E. Esarey, W.P. Leemans, Nonparaxial propagation of ultrashort laser pulses in plasma channels, Phys. Rev. E 59 (1) (1999) 1082–1095, doi:10.1103/PhysRevE.59.1082.
[38] E. Cormier-Michel, C.G.R. Geddes, E. Esarey, C.B. Schroeder, D.L. Bruhwiler, K. Paul, B. Cowan, W.P. Leemans, Scaled simulations of a 10 GeV accelerator, in: C.B. Schroeder, W.P. Leemans, E. Esarey (Eds.), Thirteenth Advanced Accelerator Concepts, Santa Cruz, CA, 2008, American Institute of Physics, Melville, NY, 2009, pp. 297–302.
[39] E. Cormier-Michel, B.A. Shadwick, C.G.R. Geddes, E. Esarey, C.B. Schroeder, W.P. Leemans, Unphysical kinetic effects in particle-in-cell modeling of laser wakefield accelerators, Phys. Rev. E 78 (1) (2008) 016404. doi:10.1103/PhysRevE.78.016404. URL: <http://link.aps.org/abstract/PRE/v78/e016404>.
[40] C.G.R. Geddes, E. Cormier-Michel, E. Esarey, C.B. Schroeder, W.P. Leemans, D.L. Bruhwiler, B. Cowan, C. Nieter, K. Paul, J.R. Cary, Scaled simulation design of high quality laser wakefield accelerator stages, in: Proceedings of the 2009 Particle Accelerator Conference, Vancouver, BC, Canada, IEEE, in press.
[41] B.A. Shadwick, C.B. Schroeder, E. Esarey, Nonlinear laser energy depletion in laser–plasma accelerators, Physics of Plasmas 16 (5) (2009) 056704. doi:10.1063/1.3124185. URL: <http://link.aip.org/link/?PHP/16/056704/1>.
[42] E.S. Sarachik, G.T. Schappert, Classical theory of the scattering of intense laser radiation by free electrons, Phys. Rev. D 1 (10) (1970) 2738–2753, doi:10.1103/PhysRevD.1.2738.
[43] P. Sprangle, E. Esarey, A. Ting, Nonlinear interaction of intense laser pulses in plasmas, Phys. Rev. A 41 (8) (1990) 4463–4469, doi:10.1103/PhysRevA.41.4463.
[44] E.A. Startsev, C.J. McKinstrie, Multiple scale derivation of the relativistic ponderomotive force, Phys. Rev. E 55 (6) (1997) 7527–7535, doi:10.1103/PhysRevE.55.7527.
[45] D. Bauer, P. Mulser, W.H. Steeb, Relativistic ponderomotive force, uphill acceleration, and transition to chaos, Phys. Rev. Lett. 75 (25) (1995) 4622–4625, doi:10.1103/PhysRevLett.75.4622.
[46] D. Bituk, M. Fedorov, Relativistic ponderomotive forces, J. Exp. Theoret. Phys. 89 (4) (1999) 640–646. URL: <http://dx.doi.org/10.1134/1.559024>.
[47] E. Esarey, M. Pilloff, Trapping and acceleration in nonlinear plasma waves, Phys. Plasmas 2 (5) (1995) 1432–1436. doi:10.1063/1.871358. URL: <http://link.aip.org/link/?PHP/2/1432/1>.
[48] K. Németh, B. Shen, Y. Li, H. Shang, R. Crowell, K.C. Harkay, J.R. Cary, Laser- driven coherent betatron oscillation in a laser-wakefield cavity, Phys. Rev. Lett. 100 (9) (2008) 095002, doi:10.1103/PhysRevLett.100.095002.